

Large Scale Simulations and Parameter Study for a Simple Recrystallization Model

Matt Elsey*, Selim Esedođlu, and Peter Smereka

Department of Mathematics, University of Michigan, Ann Arbor, MI 48109, USA

October 20, 2010

Abstract

Distance function-based diffusion generated motion, a highly efficient numerical algorithm, is used to simulate a classical model of recrystallization in unprecedented detail and in physically relevant parameter regimes not attainable with many previous techniques. The algorithm represents interfaces implicitly and is closely related to the level set method. In particular, it allows for automatic topological changes and arbitrarily large time steps. Large scale simulations of recrystallization for physically relevant parameter values are presented in detail. In addition, new analytical estimates for the distribution of surviving nuclei are obtained and compared with the numerical results.

Keywords: diffusion-generated motion, mean curvature flow, recrystallization

1 Introduction

Recrystallization is an important process for microstructural development in polycrystals, occurring when cold-worked metals are annealed. This process has been studied for over seventy years. Burke and Turnbull [6] gave a classic review of recrystallization in 1952. For a more recent review, see, e.g., Doherty et al. [9]. The cold work stores energy in the form of dislocations which are then eliminated by the growth of undeformed recrystallized grains. Recrystallization occurs in the processing of metals, both as a deliberate attempt to improve macroscale properties (such as ductility) and as an byproduct of other processing steps. As such, it is important to develop numerical techniques to simulate this phenomenon well.

In this paper, our focus is on careful numerics for a simple model of recrystallization, so that inherent, genuine features of the model can be understood in isolation from potential numerical artifacts that plague certain popular algorithms. We consider the simple, but influential, model of Srolovitz et al. [33, 34]. We present an analysis of the role of parameters in this model, and carry out detailed, large-scale, fully resolved simulations using a new, implicit (level sets-like) numerical method (fully described in [10]), distance function-based diffusion generated motion. We accomplish the following:

1. Determine the dependence of growth behavior of nuclei on distribution of nucleus sizes and nucleation rate for the model of Srolovitz et al.
2. Compare and contrast with Monte Carlo simulation results of [33, 34].
3. Simulate physical parameter regimes for this model unachievable with previous numerical methods in both two and three dimensions.
4. Show the formation of a very fine structure of elongated grains at the completion of recrystallization, unlike any other results from simulations of the model of Srolovitz et al.

*Corresponding author. Email: melsey@umich.edu

5. Demonstrate agreement of our simulations with the growth behavior analysis we perform in Section 3.3, which describes the role played by the parameters of the nucleation and recrystallization models we employ in determining the resulting microstructure.
6. Show good agreement with some pre-existing theoretical predictions.

2 Recrystallization and Nucleation Models

The recrystallization and nucleation models studied in this work are identical to the models used in the landmark papers [33, 34] by Srolovitz et al. Recrystallized grains are differentiated from unrecrystallized grains by a lower bulk energy. In three dimensions, the total energy of the system is given by:

$$E = \gamma \sum_{k < \ell} (\text{area of } \Gamma_{k\ell}) + \rho \sum_k e_k (\text{volume of } \Xi_k), \quad (1)$$

where Ξ_k denotes a grain indexed by k , $\Gamma_{k\ell}$ denotes the interface between grains Ξ_k and Ξ_ℓ , γ denotes the grain boundary energy per unit area, ρ denotes the stored energy per unit volume, and e_k is a dimensionless parameter measuring the density of dislocations within the grain Ξ_k . For simplicity, we set $e_k = 1$ for unrecrystallized grains and $e_k = 0$ for recrystallized grains, though both the model and our implementation allow for varying dislocation densities. Normal grain growth occurs in the case that e_k is equal for all grains.

For the energy given by Equation (1), the normal velocity (outward from collection k) of the interface $\Gamma_{k\ell}$ can then be written as

$$v_n(\Gamma_{k\ell}) = \mu (\gamma \kappa_{k\ell} + \rho (e_\ell - e_k)). \quad (2)$$

Here, μ denotes the grain boundary mobility. $\kappa_{k\ell}$ denotes the curvature of the interface $\Gamma_{k\ell}$, with the convention that if Σ_k were a single spherical grain of radius r surrounded by a grain Σ_ℓ , then $\kappa_{k\ell} = -2/r$. The natural, energy-minimizing boundary condition is the Herring angle condition [16]. For constant γ , the Herring condition states that triples of grains (along triple lines in three dimensions and at triple junctions in two dimensions) meet with symmetric 120° opening angles. Commonly accepted values for the stored energy and the grain boundary energy densities are $\rho = 10 \text{ MPa}$ and $\gamma = 0.5 \text{ J/m}^2$ (see, for example, the texts of Gottstein and Shvindlerman [15], page 130, and Humphreys and Hatherly [18], page 8). When recrystallization nuclei are on the length scale of $0.05 \mu\text{m}$ (so that $\kappa \approx 2 \times 10^7 \text{ m}^{-1}$), these two contributions to the normal velocity are on the same scale. However, at all length scales, the curvature term *always* has a definite, $O(1)$ effect on the evolution of the system. This effect is described further in Section 3.1.

We nondimensionalize the normal velocity using the mean initial grain radius $\langle r_0 \rangle$, derived from the mean initial grain volume $\langle V_0 \rangle$ by $\langle r_0 \rangle = (3\langle V_0 \rangle / (4\pi))^{1/3}$. We define the nondimensionalized curvature as $\kappa_{k\ell}^* = \langle r_0 \rangle \kappa_{k\ell}$. Then

$$v_n(\Gamma_{k\ell}) = \frac{\mu\gamma}{\langle r_0 \rangle} (\kappa_{k\ell}^* + \lambda (e_\ell - e_k)), \quad (3)$$

with

$$\lambda = \langle r_0 \rangle \rho / \gamma. \quad (4)$$

λ is a dimensionless parameter which weights the relative contribution of the curvature and bulk energy terms. λ then may be interpreted as choosing the physical size of the unrecrystallized grains by $\langle r_0 \rangle = \lambda \cdot 0.05 \mu\text{m}$, for the physical values of ρ and γ discussed previously. We further nondimensionalize the velocity as $v_n(\Gamma_{k\ell}) = V \cdot v_n^*(\Gamma_{k\ell})$, with velocity $V = \langle r_0 \rangle / T$, and time $T = \langle r_0 \rangle^2 / (\mu\gamma)$, so that

$$v_n^*(\Gamma_{k\ell}) = \kappa_{k\ell}^* + \lambda (e_\ell - e_k). \quad (5)$$

The normal velocity given by Equation (5) arises as gradient descent for the energy

$$E^* = \sum_{k < \ell} (\text{area of } \Gamma_{k\ell}) + \lambda \sum_k e_k (\text{volume of grain } k). \quad (6)$$

We note that the time scale T is chosen so that $t^* = 1/4$ is the time required for an isolated spherical grain of radius $\langle r_0 \rangle$ to disappear under pure curvature motion. Hereafter, we drop the \star notation and refer

solely to the nondimensionalized quantities, e.g. the energy E^* will be referred to as E . The majority of the simulations presented in this work are in two dimensions. In this case, the energy of Equation (6) still applies, with “area” replaced by “length” and “volume” by “area.”

An important feature of all recrystallization models is nucleation. In this respect, too, we shall follow the models proposed in [33] in which each spatial location is equally likely to be chosen as a nucleation site for a circular (spherical, in three dimensions) grain with a size probabilistically determined (but chosen to be small relative to the mean grain size). We observe that heterogeneities in the recrystallization pattern can arise as a consequence of the dynamics in certain length scales (in agreement with [34]). Further we shall consider two possible models for the nucleation, namely *site-saturated* and *continuous*. For site-saturated recrystallization a fixed number of grains are nucleated at the initial time and at random locations, while for continuous recrystallization grains are nucleated at a constant temporal rate at randomly chosen locations.

We apply the multiphase version of *distance function-based diffusion generated motion* fully described in [10] to simulate the evolution of the recrystallizing system under the normal velocity given by Equation (5). The basic algorithm for simulating the motion of multiple junctions by alternately constructing distance functions and applying convolutions was first proposed by Esedoglu, Ruuth, and Tsai in [12] as a variant of the threshold dynamics scheme of Merriman, Bence, and Osher [24]. Major advantages of the distance function-based algorithm include the unconditional stability, sub-grid accuracy, and computational efficiency of the method. In [11], an enhanced version of the algorithm is applied to a very large scale simulation of three-dimensional grain growth initially containing over 130,000 well-resolved grains.

Since the work of Srolovitz et al. in [33, 34], more elaborate models for recrystallization have been proposed and implemented (for example, [19, 23, 27, 28]). These models include features such as modeling of the nucleation process in greater detail, inclusion of texture-dependent grain boundary mobility and energies, and spatially dependent stored energies. Extending our numerical algorithms to such models is a direction for future work. However, our improved capacity to faithfully simulate partial differential equation (PDE) models of the form of Equation (5) already sheds new light on simulations of recrystallization. The properties of our algorithm allow for large-scale simulations far beyond those already performed, in physical parameter regimes that other models cannot attain.

3 Importance of Surface Tension to the Model

In this section, we explain how the surface tension term in Equation (5) *always* makes a significant contribution to the evolution of the system, even when the bulk energy term would seem to dominate (i.e. as $\lambda \rightarrow \infty$). We discuss three major consequences:

1. In the absence of surface tension, it has been demonstrated by Reitich and Soner [30] that the evolution is not uniquely defined. In Section 3.1, we discuss two possible solutions for a given initial condition under pure bulk energy motion. Reitich and Soner note that one of these solutions naturally arises from Equation (5) as $\lambda \rightarrow \infty$ (with time appropriately rescaled).
2. For any choice of λ , the surface tension and bulk energy contributions of Equation (5) are equal at some length scale, possibly at the length scale on which nucleation occurs in primary recrystallization. We discuss the relationship between λ and critical sizes for nuclei survival in Section 3.2.
3. The terms “homogeneous” and “heterogeneous nucleation” are used in [33, 34] to describe the spatial arrangement of surviving nuclei in simulations of primary recrystallization. In Section 3.3, we present analytical predictions for the location of successful nuclei as a function of λ (which scales the surface tension and bulk energy terms of Equation (5)) and distribution of nuclei sizes.

3.1 Importance of Curvature for Large λ

In the absence of the surface tension term in Equation (5), there is no need for the evolution to respect the Herring angle condition. However, Reitich and Soner [30] demonstrate that the evolution is not uniquely defined in this case. For example, consider Figure 1 in the case of pure bulk energy motion. Let $e_1 = 0$ and $e_2 = e_3 = 1$, so that set Σ_1 (as labeled in Figure 1(a)) grows symmetrically into sets Σ_2 and Σ_3 . Figure 1(b) shows two potential solutions. The original interfaces Γ_{12} and Γ_{13} move outwards in their respective normal

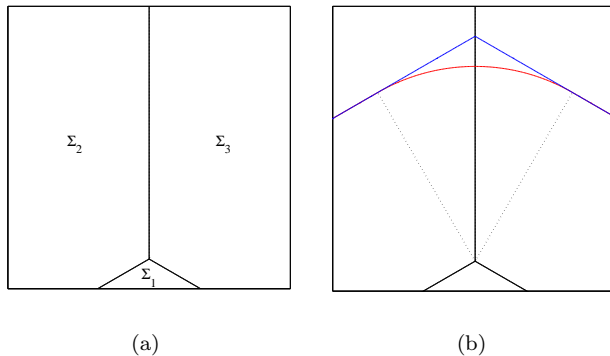


Figure 1: The initial condition in (a) evolves by pure bulk energy motion. Two possible solutions to the non-unique motion are shown in (b), one in red, the other in blue. The red curve, consisting of a circular arc connecting two straight line segments, depicts the *arrival time dynamics* solution. The blue curve, which maintains the original angle condition at the triple junction throughout the evolution, represents the *vanishing surface tension* solution of Reitich and Soner [30]. Thus, even in the limit $\lambda \rightarrow \infty$, the mere presence of curvature effects (which always dominate in a small enough neighborhood of the triple junction) has $O(1)$ effect on the dynamics regardless of how large λ is in Equation (5), thereby selecting a specific pure bulk energy motion solution from a multitude of possibilities in the limit $\lambda \rightarrow \infty$.

directions with constant velocity λ . Between the dotted lines, the classical solution does not exist. There is more than one reasonable way to propagate the solution in this region. The red path connects the unique regions by a circular arc. We call this the *arrival time dynamics* solution, and was proposed and investigated by Taylor in [35]. On the other hand, the blue path indicates another possible solution to gradient flow under pure bulk energy. Unlike in arrival time dynamics, this one maintains the initial angle at the triple junction throughout the evolution. In [30], Reitich and Soner show that this second solution arises as the limit of unique (well-defined) flows under the interfacial velocity of Equation (5) in the limit that $\lambda \rightarrow \infty$ (and with time appropriately rescaled). In other words, this second solution, called the *vanishing surface tension limit*, is the one selected from among multiple possible solutions. We maintain that the vanishing surface tension limit solution is the appropriate physical solution for grain boundary motion, as some surface tension must *always* be present, though it may be dominated by other effects. Given the $O(1)$ difference between these two candidate solutions, it is worth repeating that the surface tension plays a defining role on the dynamics even in the limit that bulk energy effects would seem to dominate, as observed in, e.g., the late stages of recrystallization.

In the recent paper [5], the authors claim to simulate pure bulk energy motion using a finite elements implementation of the level set method. Their method seems to capture the arrival time dynamics solution (the red arc in Figure 1(b)) described above; see, e.g., Figure 7 in [5]. In this section, we demonstrate that with our algorithm — diffusion generated motion — we capture the *vanishing surface tension* limit by taking large values of λ in Equation (5). Figure 2 shows the convergence of our algorithm as $\Delta x, \Delta t \rightarrow 0$ as $\lambda = 8, 16, \text{ and } 32$. Table 1 contains the convergence test data. The predictions for the final locations of the interface were calculated by finding the intersection of the two lines determined by advancing the interfaces Γ_{12} and Γ_{13} with velocity λ for the simulation time $5/1024$. These values were calculated to be 0.5451, 0.5902 and 0.6804, for $\lambda = 8, \lambda = 16, \text{ and } \lambda = 32$, respectively. These simulations are quite accurate, with relative errors under 5% for $n = 64$ grid points and under 2% for $n = 256$ grid points. The grid discretizes $[0, 1]^2$. We note that λ acts as a stiffness parameter: increasing λ requires increased computational effort for fixed accuracy. Even in the extreme case, $\lambda = 32$, the triple junction moves only between 0.5 and 0.75 on the vertical axis, suggesting that good accuracy is achieved for motions using only about one-fourth the available grid points in each direction. The convergence rate is sublinear but agrees well with convergence rates seen at triple junctions for pure curvature motion via the same algorithm in [12].

Furthermore, the surface tension plays a decisive role even in the limit that it vanishes in determining the

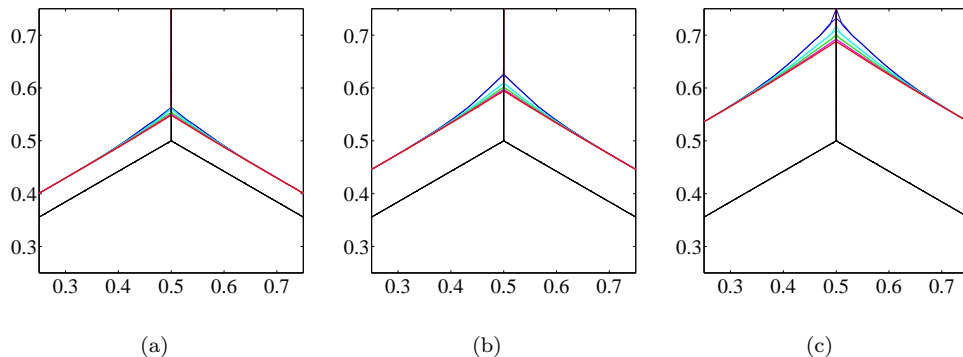


Figure 2: Comparisons with the vanishing surface tension limit (a translation of the black initial curve) as Δx and Δt are refined in our algorithm for motion by Equation (5) with (a) $\lambda = 8$, (b) $\lambda = 16$, and (c) $\lambda = 32$. The computed solution at successively higher resolutions are shown in blue, cyan, green, magenta, and red, respectively.

Δx	nt	$\lambda = 8$			$\lambda = 16$			$\lambda = 32$		
		Y_f	% Err.	C.R.	Y_f	% Err.	C.R.	Y_f	% Err.	C.R.
1/32	50	0.5630	3.28%	—	0.6259	6.04%	—	0.7323	7.62%	—
1/64	100	0.5599	2.72%	0.27	0.6094	3.25%	0.90	0.7090	4.21%	0.86
1/128	200	0.5539	1.60%	0.76	0.6016	1.92%	0.76	0.6989	2.72%	0.63
1/256	400	0.5504	0.97%	0.72	0.5973	1.20%	0.68	0.6922	1.73%	0.65
1/512	800	0.5485	0.61%	0.67	0.5947	0.76%	0.67	0.6881	1.13%	0.62

Table 1: Errors in approximating the vanishing surface tension limit using diffusion generated motion. The grid discretizes $[0, 1]^2$ with steps of Δx , and nt denotes the number of time steps used to simulate the total time $5/1024$. Y_f denotes the final vertical position of the interface. % Err. denotes the percentage error from the predicted location. C.R. denotes the convergence rate, computed as $\log_2(\text{Error using } n/2 \text{ grid points} / \text{Error using } n \text{ grid points})$.

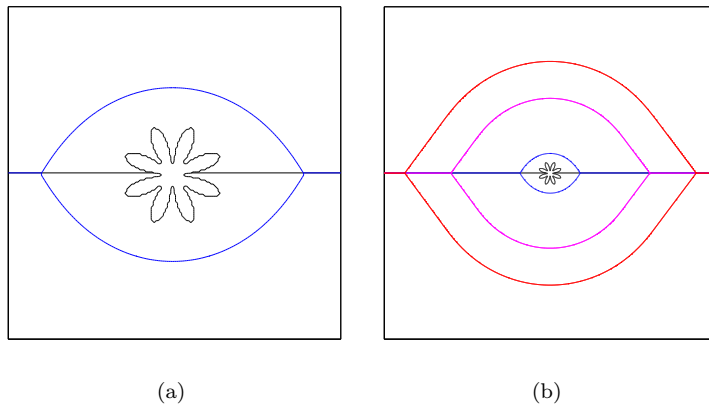


Figure 3: Any initial shape which is sufficiently large for the choice of λ will grow; and as the ratio $\lambda/\kappa \rightarrow \infty$ will approach the characteristic shape described by Equation (7). In contrast, arrival time dynamics predict the asymptotic shape to be a disk, demonstrating again the $O(1)$ difference between the two possible definitions of a solution. The initial condition is zoomed in on in (a). Later times in the evolution are shown in (b), with the characteristic shape of circular arcs connected by line segments seen clearly.

characteristic shape of recrystallized nuclei growing along pre-existing grain boundaries. Rather than the nucleus appearing as a growing circle overlapping the pre-existing boundary (as in solutions computed in [5]), the nucleus takes on an elongated shape along the boundary, as in Figure 3. This shape can be derived as a self-similar solution for pure bulk energy motion respecting the Herring angle condition at triple junctions. It is described as a function of the circular sector radius r by:

$$y(x; r) = \begin{cases} \pm\sqrt{r^2 - x^2}, & |x| \leq \frac{\sqrt{3}r}{2} \\ \pm\sqrt{3} \left(x \pm \frac{\sqrt{3}r}{2} \right) \pm \frac{r}{2}, & \frac{\sqrt{3}r}{2} \leq |x| \leq \frac{2r}{\sqrt{3}} \end{cases} \quad (7)$$

This shape is *independent* of the choice of λ : as long as a nucleus along a pre-existing boundary survives and grows, it will penetrate the existing unrecrystallized grains. The aspect ratio of the shape is $2 : \sqrt{3}$. In contrast, the arrival time dynamics solution has the disk as its characteristic shape, regardless of the pre-existing structure beneath the nucleus. We demonstrate that our algorithm evolves towards the self-similar solution even from a highly complex initial condition that does not respect the boundary conditions, as shown in Figure 3.

3.2 Critical Nuclei

For the model considered in this work, the curvature term contributes at the same order as the bulk energy term on the length scale $1/\lambda$; this is just a simple fact of the scaling in Equation (5). One of the appealing attributes of this model developed by Srolovitz et al. in [33, 34] is the potential for capturing various recrystallization phenomena, e.g. homogeneous or heterogeneous nucleation, through the effect surface tension may play at the scale of the smallest recrystallized embryos. An exact, though unstable, stationary solution is easily determined from Equation (5) for any λ . These critical nuclei are those with constant curvature $\kappa = -1/\lambda$ away from triple junctions, with 120° angles at all triple junctions. Thus the stationary boundary must always be the union of circular arcs. As in the case of pure bulk growth, the stationary shapes have aspect ratios independent of λ . We consider three cases: (1) a nucleus contained entirely within another grain, (2) lying on a grain boundary, and (3) lying on a triple junction. We further assume that the nucleus is small compared to the original grains and make the two following approximating assumptions: the pre-existing grains have straight boundaries, and the nucleus lies with its center on the grain boundary or triple junction, as appropriate.

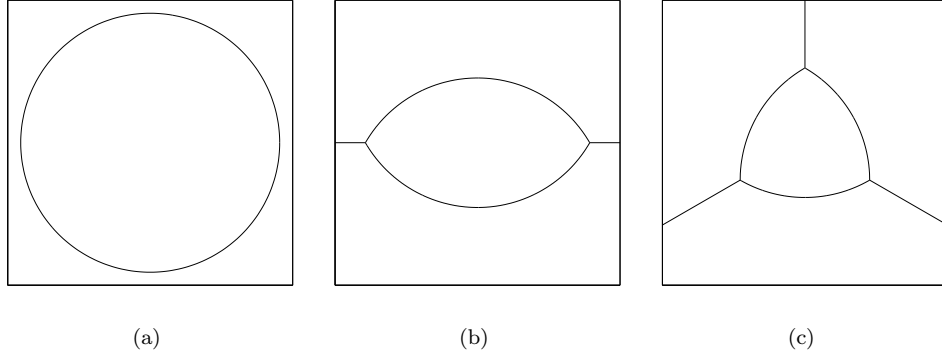


Figure 4: The critical shapes corresponding to cases 1 (grain interior), 2 (grain boundary) and 3 (triple junction), respectively. The shapes are independent of λ , while their areas scale with λ^{-2} .

Case (1) is trivial: The grain is a circle of radius $r = 1/\lambda$, with area $A_1(\lambda) = \pi\lambda^{-2}$. For case (2), assume the grain boundary lies along the line $y = 0$. Then the shape is implicitly represented as

$$\begin{cases} x^2 + \left(y + \frac{1}{2\lambda}\right)^2 = \lambda^{-2}, & y > 0, \\ x^2 + \left(y - \frac{1}{2\lambda}\right)^2 = \lambda^{-2}, & y < 0, \end{cases} \quad (8)$$

with area $A_2(\lambda) = \left(\frac{2\pi}{3} - \frac{\sqrt{3}}{2}\right)\lambda^{-2}$. Finally, we may rotate the triple junction of case (3) so that the grain boundaries emanate along the rays $\theta = \pi/2, 7\pi/6$ and $11\pi/6$. This shape is given by:

$$\begin{cases} \left(x + \frac{1}{2\lambda}\right)^2 + \left(y + \frac{1}{2\sqrt{3}\lambda}\right)^2 = \lambda^{-2}, & \theta \in \left(-\frac{\pi}{6}, \frac{\pi}{2}\right), \\ \left(x - \frac{1}{2\lambda}\right)^2 + \left(y + \frac{1}{2\sqrt{3}\lambda}\right)^2 = \lambda^{-2}, & \theta \in \left(\frac{\pi}{2}, \frac{7\pi}{6}\right), \\ x^2 + \left(y - \frac{1}{\sqrt{3}\lambda}\right)^2 = \lambda^{-2}, & \theta \in \left(\frac{7\pi}{6}, \frac{11\pi}{6}\right), \end{cases} \quad (9)$$

with area $A_3(\lambda) = \left(\frac{\pi - \sqrt{3}}{2}\right)\lambda^{-2}$. These shapes are shown in Figure 4. Note the constant curvature in smooth regions and that the Herring condition is satisfied at triple junctions.

We define the critical grain radii to be the effective grain radius of the critical shape, $R_i = \sqrt{A_i(\lambda)/\pi}$, and calculate these from to be:

$$R_i = \begin{cases} \frac{1}{\lambda}, & i = 1, \\ \frac{\sqrt{2/3 - \sqrt{3}/(2\pi)}}{\lambda}, & i = 2, \\ \frac{\sqrt{1/2 - \sqrt{3}/(2\pi)}}{\lambda}, & i = 3. \end{cases} \quad (10)$$

Thus $R_2 \approx .6253/\lambda$ and $R_3 \approx .4736/\lambda$, for any choice of λ . We conclude that for fixed λ , *the critical grain size necessary for nucleus survival is smallest at triple junctions, moderate at grain boundaries, and largest in grain interiors*. This observation has been verified experimentally and in simulations by numerous previous authors.

3.3 Parameter Regimes

In this section, we give a complete classification of the role of parameters in the nucleation and recrystallization model used here and in the work of Srolovitz et al. [33, 34] with regard to their effect on the type of recrystallization (homogeneous or heterogeneous) that results. The understanding developed here will guide our numerical experiments with the model in subsequent sections.

Let R be the (random) size of a circular nucleus, given by some distribution f_R , and let T_i be the event that a nucleus touches exactly i different grains (corresponding to the cases of Section 3.2). To approximate the conditional probability $\mathbb{P}(T_i|R = r)$, we note the following facts:

- The total area of the nondimensionalized domain D is $|D| = \pi N_0$, where N_0 is the initial number of unrecrystallized grains.
- Assuming grains are approximately circular, the total boundary length is πN_0 , as each individual grain has boundary length 2π , and each segment of grain boundary is counted by two grains.
- One implication of the von Neumann area law [25] is that the mean number of triple junctions along the boundary of one grain must be 6. Thus the number of triple junctions in the system must be $2N_0$, as each triple junction is counted by three grains.
- A nucleus of radius r must have its center within r units of a grain boundary or a triple junction in order to be touching 2 or 3 different grains, respectively.

We define $D_i \subset D$, for $i = 1, 2, 3$, to be region where a nuclei of radius r touches exactly i pre-existing grains. Thus D_3 , the region in which a grain of radius r must be centered to touch a triple junction, has $|D_3| \approx 2N_0 \cdot \pi r^2$. Similarly, we conclude from the total boundary length that $|D_2 \cup D_3| \approx \pi N_0 \cdot 2r$. Since $D_2 \cap D_3 = \emptyset$, we conclude that

$$\mathbb{P}(T_i|R = r) \approx \begin{cases} 1 - 2r, & i = 1, \\ 2(r - r^2), & i = 2, \\ 2r^2, & i = 3, \end{cases} \quad (11)$$

if nuclei are placed uniformly at random within D .

Further let G be the event that a given nucleated grain grows. Numerically, we find that the critical radii for initially circular nuclei are very close to the values found analytically for the critical shapes described in Section 3.2:

$$R_i \approx \begin{cases} \frac{1}{\lambda}, & i = 1, \\ \frac{.642}{\lambda}, & i = 2, \\ \frac{.484}{\lambda}, & i = 3. \end{cases} \quad (12)$$

To further validate this numerical result, we consider nuclei which are initially circular. In this case, we can give an upper bound on the critical radii as $R_2 \leq 2/(3\lambda)$ and $R_3 \leq 1/(2\lambda)$. This follows from the expression for the rate of change of area of a recrystallizing grain Σ :

$$\frac{dA}{dt} = \frac{\pi}{3}(N_e - 6) + \lambda \text{Per}(\Sigma), \quad (13)$$

where N_e is the number of edges (equivalently, the number of neighboring grains) of grain Σ . The isoperimetric inequality guarantees that if $dA/dt \geq 0$ for some time interval $[0, t^*]$, then $\text{Per}(\Sigma(t^*)) \geq \text{Per}(\Sigma(0))$, as the circular initial condition has minimal perimeter among all shapes with area $\geq A(0)$. Thus, choosing the critical radii above guarantees that $dA/dt \geq 0$ for all subsequent times. Equation (13) shows that the critical nucleus size depends only on the perimeter of the nucleus and the *number* of grains neighboring the nucleus; but is independent of *where* on the nucleus the triple junctions occur. We numerically verified that the critical grain size is minimally affected by varying where the nucleus touches the grain boundary or triple junction, finding a difference of approximately 0.2% in critical grain radii for circles nucleated with their centers at the grain boundary (as in Figure 5(a)) as compared to circles nucleated so that the grain boundary is near the edge of the nucleus (see Figure 5(b)).

Therefore we have

$$\mathbb{P}(G \cap T_i|R = r) = \begin{cases} \mathbb{P}(T_i|R = r), & r > R_i \\ 0, & r < R_i, \end{cases} \quad (14)$$

where R_i is given by Equation (12). Then we can compute

$$\mathbb{P}(G \cap T_i) = \int_{-\infty}^{\infty} \mathbb{P}(G \cap T_i|R = r) f_R(r) dr = \int_{R_i}^{\infty} \mathbb{P}(T_i|R = r) f_R(r) dr. \quad (15)$$

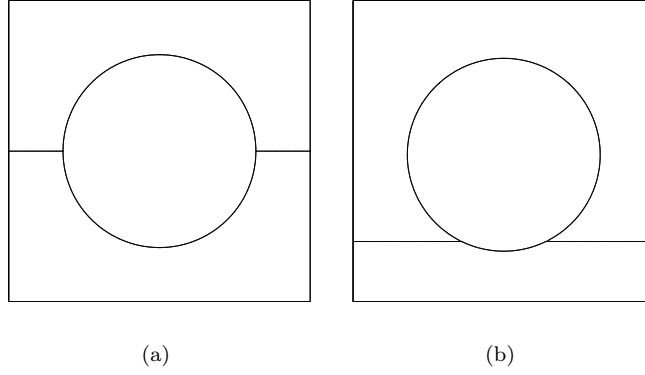


Figure 5: The critical grain size for circular nuclei is found analytically and numerically to be independent of where on the nucleus the grain boundary crosses, either (a) at nucleus center, or (b) near the edge of the nucleus.

It is surely of interest to describe the locations of nuclei that will survive in this model. The conditional probabilities describing the distribution of surviving nuclei locations is given by:

$$\mathbb{P}(T_i|G) = \frac{\mathbb{P}(G \cap T_i)}{\sum_{i=1}^3 \mathbb{P}(G \cap T_i)}. \quad (16)$$

An instructive first case is to suppose that the nucleation radius R is deterministic, i.e. $f_R(r) = \delta(r - \mu)$, where δ denotes the Dirac delta. Then there are four cases:

1. $\mu > R_1 > R_2 > R_3$: Grain grow regardless of where they are placed, and

$$\mathbb{P}(T_i|G) = \begin{cases} 1 - \mu, & i = 1, \\ 2(\mu - \mu^2), & i = 2, \\ 2\mu^2, & i = 3. \end{cases} \quad (17)$$

2. $R_1 > \mu > R_2 > R_3$: Grains only grow along grain boundary or at triple junctions, with

$$\mathbb{P}(T_i|G) = \begin{cases} 0, & i = 1, \\ 1 - \mu, & i = 2, \\ \mu, & i = 3. \end{cases} \quad (18)$$

3. $R_1 > R_2 > \mu > R_3$: Grains grow only at triple junctions. $\mathbb{P}(T_3|G) = 1$.

4. $R_1 > R_2 > R_3 > \mu$: Grains do not grow. Recrystallization cannot occur in the absence of phenomena beyond the scope of the approximations made here (for example, the presence of quadruple or higher-order junctions, severely kinked grain boundaries, or interactions between nuclei).

These cases partition the μ – R_1 parameter space into four regions, as shown in Figure 6.

More generally, one might suppose that the grain radii are approximately normally distributed with some mean μ and variance σ^2 . Taking care to ensure that $R > 0$, we define the nonnegative normal distribution \bar{N} by

$$f_X(x) = \begin{cases} \frac{1}{\Phi(\mu/\sigma)} \left(\frac{1}{\sqrt{2\pi\sigma^2}} \exp\left(\frac{-(x-\mu)^2}{2\sigma^2}\right) \right), & x \geq 0, \\ 0, & x < 0, \end{cases} \quad (19)$$

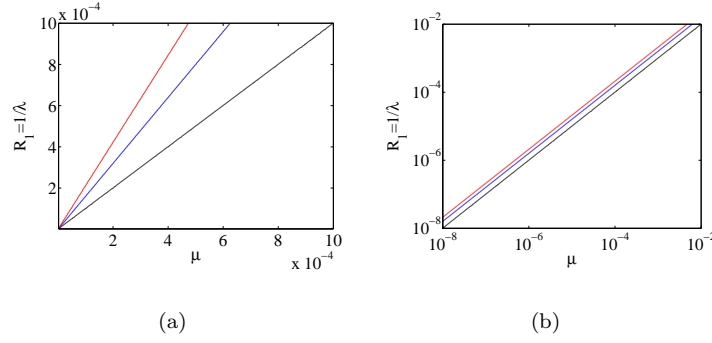


Figure 6: The μ — R_1 parameter space for deterministic nucleation sizes divides into four regions describing whether the recrystallization is homogeneous (equally likely to occur anywhere throughout D), heterogeneous (along grain boundaries), heterogeneous (only at triple junctions), or will not occur (as R_1 increases for constant μ , respectively). On (a) linear and (b) logarithmic axes.

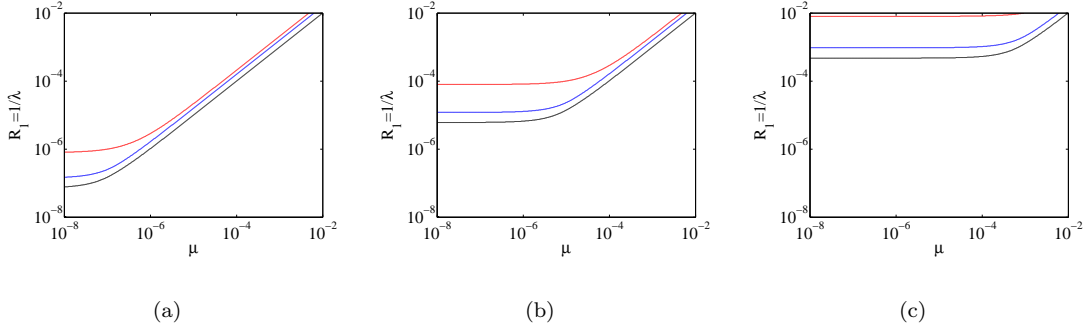


Figure 7: The μ — R_1 parameter space for (a) $\sigma = 10^{-8}$, (b) $\sigma = 10^{-6}$ and (c) $\sigma = 10^{-4}$. Increasing σ increases the likelihood of large nucleations, allowing a greater part of the region to support homogeneous nucleation. The contours bounding other regions move in a similar fashion.

if $X \sim \bar{N}(\mu, \sigma^2)$, where $\Phi(x)$ is the cumulative distribution function for the standard normal distribution, $N(0, 1)$. Suppose $R \sim \bar{N}(\mu, \sigma^2)$. Then we calculate that

$$\mathbb{P}(G \cap T_i) \approx \begin{cases} \frac{1}{\Phi(\mu/\sigma)} \left\{ (1 - 2\mu) \left[1 - \Phi\left(\frac{R_1 - \mu}{\sigma}\right) \right] - \sigma \sqrt{\frac{2}{\pi}} \exp\left(\frac{-(R_1 - \mu)^2}{2\sigma^2}\right) \right\}, & i = 1, \\ \frac{1}{\Phi(\mu/\sigma)} \left\{ 2(\mu - \mu^2 - \sigma^2) \left[1 - \Phi\left(\frac{R_2 - \mu}{\sigma}\right) \right] + \sigma \sqrt{\frac{2}{\pi}} (1 - R_2 - \mu) \exp\left(\frac{-(R_2 - \mu)^2}{2\sigma^2}\right) \right\}, & i = 2, \\ \frac{1}{\Phi(\mu/\sigma)} \left\{ 2(\mu^2 + \sigma^2) \left[1 - \Phi\left(\frac{R_3 - \mu}{\sigma}\right) \right] + \sigma \sqrt{\frac{2}{\pi}} (R_3 + \mu) \exp\left(\frac{-(R_3 - \mu)^2}{2\sigma^2}\right) \right\}, & i = 3. \end{cases} \quad (20)$$

We visualize the effects of parameter choice in the μ — R_1 plane for various values of σ in Figure 7. Compare to Figure 6(b). Increasing σ increases the probability of nucleations with $R > \mu$, allowing homogeneous nucleation to prevail even for $\mu < R_1$. In the regions of parameter space where μ and R_1 are much larger than σ , the behavior is as predicted in the deterministic case.

Figures 6 and 7 show that there are two very distinct parameter regimes: $\mu \ll \sigma$, and $\mu \gg \sigma$. In the first, $\mu \ll \sigma$, there is a wide range of values R_1 for which heterogeneous nucleation (nuclei survival primarily along grain boundaries) may occur. In contrast, when $\mu \gg \sigma$, nuclei radii are essentially deterministic, and the parameter regime in which heterogeneous nucleation may occur is much more narrow. In this case, there must be a close relationship between R_1 and μ in order for heterogeneous nucleation to occur. As

heterogeneous nucleation is frequently observed in practice, it appears reasonable that either $\sigma \gg \mu$ or that there is indeed a close physical relationship between μ and $R_1 = 1/\lambda$.

4 Comparison to Previous Work

For the recrystallization model studied here, there are very few theoretical predictions available compared with, e.g., models of normal grain growth. Primary among the known results is the theory of Johnson and Mehl [21], Avrami [2–4], and Kolmogorov [22] (JMAK) for the kinetics of the recrystallized volume fraction F . The JMAK theory is briefly discussed in Section 4.1. In contrast, there is an abundance of numerical simulation studies of recrystallization in the literature. Many of the most recent numerical works focus on incorporating additional features such as texture dependence and physically-based nucleation models. Our focus is different: we stay with the simple model of Srolovitz et al., and explore instead the difference that fully resolved numerics — as opposed to additional physics — makes. Once again, this is in the interest of separating numerical issues (possibly artifacts) from modeling issues. As such, in Section 4.2 we compare our numerical results with prior simulations of the Srolovitz model, in particular with the Monte Carlo simulations contained in the original papers [33,34].

4.1 JMAK Theory

A normal interface velocity of the form given by Equation (5), in the limit $\lambda \rightarrow \infty$, is in keeping with the JMAK theory. This theory is based on the assumption that each nucleated grain grows outward with constant normal velocity, which occurs in our system by neglecting the curvature term, and is approximated by choices of length scale with grains sufficiently large that the bulk energy term dominates the interfacial energy term in Equation (5). The JMAK model has associated theoretical results in this limit, predicting the recrystallized volume fraction F to be a sigmoidal function of time, t , in the form

$$F(t) = 1 - \exp(-kt^p), \quad (21)$$

where k and p are constant. The parameter p can be predicted given the nucleation technique and the dimensionality of the evolution ([7], page 542).

4.2 Monte Carlo Simulations

A variety of numerical techniques have been employed previously in simulations of recrystallization. Chief among them are the Monte Carlo Potts [33,34] and cellular automata [17] techniques. Both have well-known shortcomings (see, for example, [18], page 422, and [20], page 102). More recently, there are hybrid methods that combine the two [31], as well as a level sets-based implementation [5] of pure bulk energy (recrystallization) dynamics, disregarding angle conditions. The seminal works [33,34] by Srolovitz et al. both introduced the models we study in this work and carried out Monte Carlo simulations in two dimensions. As an important first step in verifying our algorithms, we demonstrate in this section reasonable agreement between our results and those of [33,34] in certain parameter regimes. However, we have also observed important differences; we believe these are due to the benefits of our improved numerics and constitute the content of Section 5, where they are extensively reported and discussed.

In [33,34], the authors introduce the parameters H and J , corresponding to scalings for stored (bulk) energy and interfacial energy. They use the ratio H/J in place of our nondimensionalized parameter λ , with the correspondence

$$\lambda = \frac{H}{J} \sqrt{\frac{\langle g \rangle}{\pi}}, \quad (22)$$

where $\langle g \rangle$ is the mean number of grid points per grain in the initial (unrecrystallized) microstructure. Every simulation in [33] and [34] uses the same initial microstructure, with $\langle g \rangle \approx 43$ and approximately 930 initial unrecrystallized grains, resulting in $\lambda \approx 3.7H/J$. The nuclei were taken to be 1 site for $H/J = 5$ and 3, and 3 sites for $H/J = 2, 1.5, 1$ and 0.5 on a 200×200 triangular grid. These correspond to nondimensionalized areas of 0.0730 and 0.2191, respectively, with equivalent radii of 0.1525 and 0.2641 (recall that the mean equivalent radius of an unrecrystallized grain is 1). These parameter choices are plotted in Figure 8 on

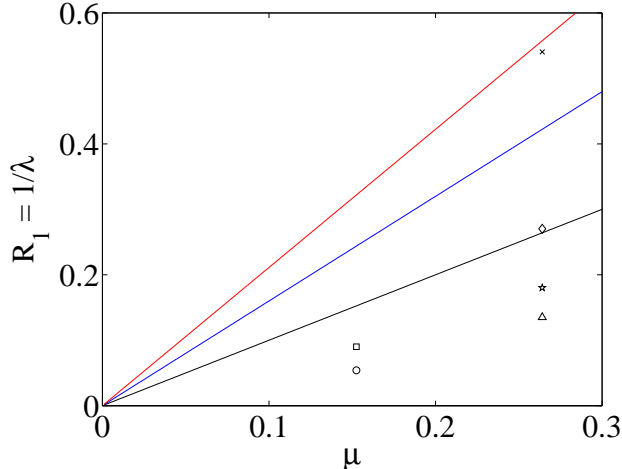


Figure 8: The deterministic μ – R_1 parameter space with the simulations of [33, 34] marked. $\lambda = 18.5, 11.1, 7.4, 5.55, 3.7$ and 1.85 correspond to circle, square, triangle, star, diamond and x markers, respectively. Note that the simulations with $\lambda = 7.4$ and 5.55 correspond to homogeneous nucleation for this model, not heterogeneous nucleation as is found by the Monte Carlo simulations.

the μ – R_1 parameter space as discussed in Section 3.3. Note that for $\lambda = 7.4$ and 5.55 (corresponding to $R_1 = 0.1351$ and $R_1 = 0.1802$, respectively), the parameter choices fall in the homogeneous nucleation range under our analysis. Srolovitz et al. characterize these parameter choices (for them, $H/J = 2$ and 1.5 , with 3 site nuclei) as heterogeneous nucleation. The model of Section 3.3 suggests that the effects seen in [34] for these parameter choices are an effect of the Monte Carlo simulation technique rather than an outcome determined by the model of Equation (6).

We will now focus on the simulations of site-saturated nucleation performed in [33, 34]. Our simulations were performed for 200, 100, 50, 20, 10 and 5 nuclei at $\lambda = 18.5$ and $\lambda = 11.1$, and for 2000, 1000, 500, and 200 nuclei at $\lambda = 7.4, 5.55, 3.7$, and 1.85 , agreeing with the simulations of [33, 34]. Figure 9 examines the microstructure for 200 nuclei, with radius $\mu = 0.2641$. Figure 9(a) shows part of the microstructure at $t = 0$, immediately after 200 nuclei are added to the domain. Figures 9(b) and (c) show the microstructure for $\lambda = 7.4$ and $\lambda = 5.55$ at $t = 0.557$. In these simulations, it is clear that *all* nuclei are growing, agreeing with the prediction of homogeneous growth shown in Figure 8. For $\lambda = 3.7$, the chosen nucleation size is very near the border of homogeneous growth and grain boundary-dominated growth. It can be seen in Figure 9(d) that for this parameter choice, grains nucleated in grain interiors remain approximately stationary, while grains nucleated on grain boundaries and at triple junctions grow. Note that the theory of Section 3.3 does not account for the rate at which grains grow or shrink, or impingement between nucleating grains. In these simulations, impingement will occur before some of the nuclei in grain interiors disappear. In Figure 9(e), grains which nucleate in grain interiors disappear quickly, with all completely gone by $t = 0.1115$. Grains which nucleated along grain boundaries persist longer but again have all vanished by $t = 0.2229$. At this time only recrystallizing grains which nucleated at triple junctions remain, agreeing with the prediction shown in Figure 8 for $\lambda = 1.85$.

Figure 10 demonstrates the time evolution of the recrystallized area fraction F for simulations of site-saturated recrystallization with varying values of $\lambda \in [1.85, 18.5]$ and varying numbers of recrystallization nuclei (from 5 to 2000), corresponding precisely to the parameter choices of Figures 6 and 7 in [33] and those of Figures 8 and 9 in [34]. The essential features of our plots match the corresponding ones in [33, 34]. Figure 10(b) visualizes the Avrami exponent p of Equation (21). The JMAK prediction can be rearranged as $\log(-\log(1-F)) = p \log t + \log k$, suggesting that these plots should have slope p on logarithmic axes, where p is predicted to be 2 for two-dimensional site-saturated nucleation ([7], page 542). Triangles with slope 2 are inset on the Avrami plots and agree well with the trends of the plots at intermediate times. Note that the JMAK prediction is approximate for this model, neglecting the influence of curvature, which is strongest

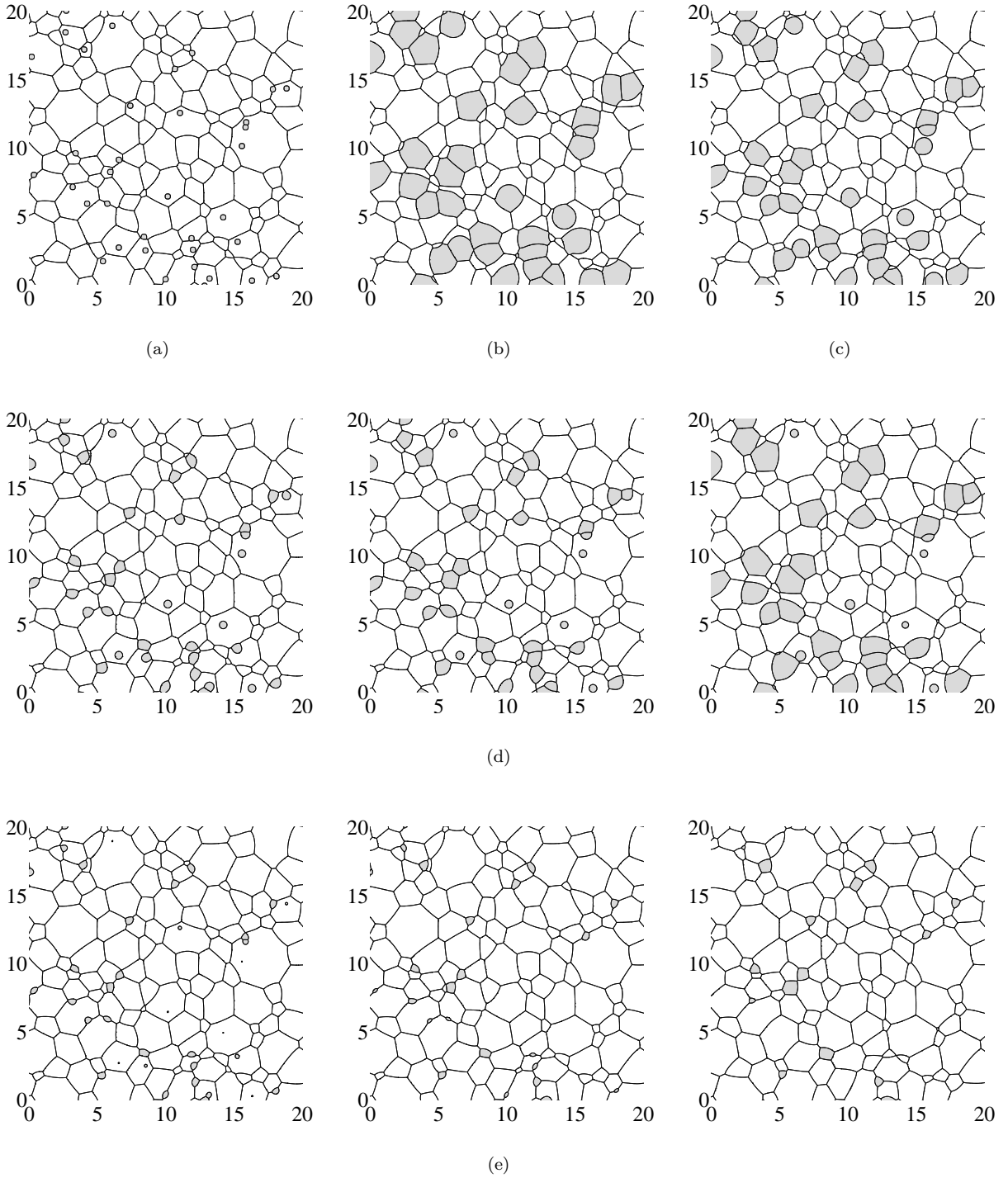


Figure 9: Snapshots of microstructure for site-saturated nucleation, with 200 nuclei of radii 0.2641 and varying λ . (a) Nuclei immediately after nucleation. (b) $\lambda = 7.4$ at $t = 0.0557$. (c) $\lambda = 5.55$ at $t = 0.0557$. In both (b) and (c), all nuclei survive and grow: homogeneous nucleation. (d) $\lambda = 3.7$ at $t = 0.0557, 0.1115,$ and 0.2229 , respectively. Nuclei crossing grain boundaries and triple junctions clearly grow, while nuclei in grain interiors appear to remain approximately stationary. (e) $\lambda = 1.85$ at the same times as (d). Nuclei away from triple junctions all disappear quickly.

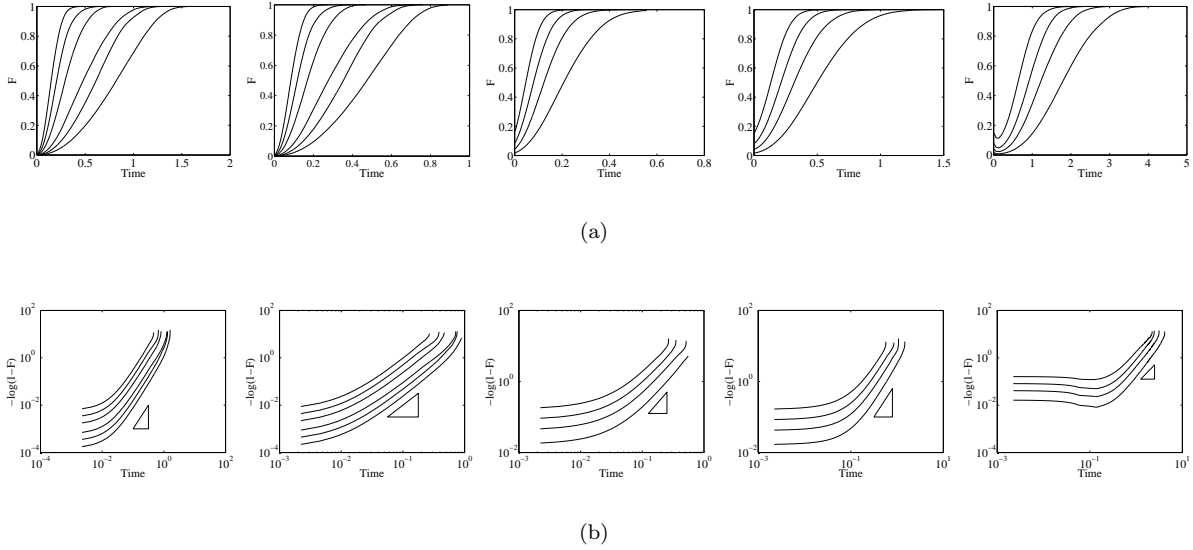


Figure 10: (a) The recrystallized area fraction F for $\lambda = 18.5, 11.1, 7.4, 5.55, 3.7$ and 1.85 , respectively. The curves correspond to 200, 100, 50, 20, 10, and 5 nuclei (from left to right) in the first two plots, and to 2000, 1000, 500, and 200 nuclei in the last three. Corresponds to Figure 6 of [33] and Figure 8 of [34]. (b) The Avrami plots for the same experiments, corresponding to Figure 7 of [33] and Figure 9 of [34]. The slope of two is predicted for two-dimensional site-saturated nucleation.

on small recrystallizing grains, present early in the evolution.

The evolution of the mean recrystallized grain area for simulations with $\lambda = 18.5$ and 11.1 is shown in Figure 11(a). As expected (see, for example, [33]), $\langle A \rangle$ increases with t^2 at intermediate times, when the effect of curvature on recrystallized grain size is small but the recrystallized grains do not impinge on each other frequently. At later times in the evolution, the mean growth rate of recrystallized grains slows due to impingement. This plot agrees well with Figure 8 of [33] up to scaling factors in time and total area.

Figure 11(b) gives the grain size distribution function for recrystallized grains in the simulation with $\lambda = 3.7$ and 2000 site-saturated nuclei at the time when an area fraction of $F = 0.9$ is reached, while Figure 11(c) gives the distribution of N_e sided recrystallizing grains, and Figure 11(d) gives the mean normalized size of N_e sided grains for these same conditions. The plots should be compared to Figures 10, 11, and 12 of [34]: the parameters of our and their simulations matched exactly. Some differences are striking. For example, we find the peak of the topological (number of edges) distribution to fall at $N_e = 5$ (Figure 11(c)), while Figure 11 of [34] shows the peak of this distribution to fall at $N_e = 4$. Our results find a much smaller proportion of four-sided grains than any of five-, six- or seven-sided grains. Figure 11(d) displays an approximately linear relationship between the topological class (number of edges) of a grain and the mean normalized grain radius for grains of that topological class, in disagreement with the simulation results of [34], which show some nonlinearities for small and large N_e (see Figure 12 of [34]). Also, the peak of the grain size distribution is to the right of 1 in the present simulations (Figure 11(b)), while it is to the left of 1 in the Monte Carlo simulations. However, the sample size is small and the distributions are not well resolved, so one must be cautious in making conclusions about the cause of these observations. The major observation made in [34] about Figure 10 of that work holds in Figure 11(b): the maximum grain size is not more than twice the mean among recrystallizing grains. In contrast, this ratio is seen in grain growth to be between 2.5 and 3.

Following [33,34], we also perform simulations under continuous nucleation conditions. At each time step, we nucleate grains at locations uniformly chosen in the microstructure, but remove nuclei placed at already-recrystallized locations. Thus the effective nucleation rate declines as recrystallization proceeds due to the decrease in area available for nucleation. It is difficult to relate our nondimensionalized time to the Monte

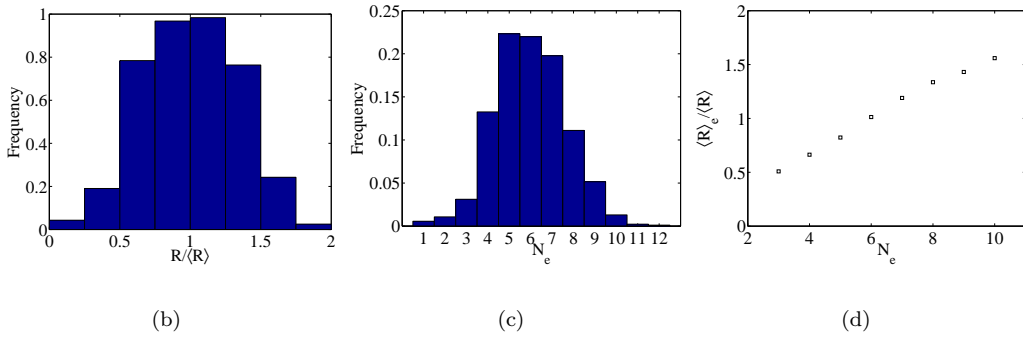
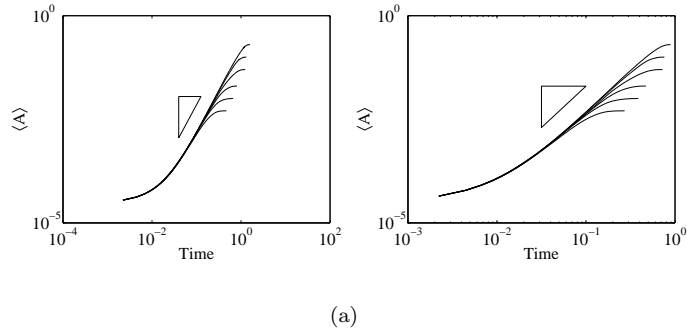


Figure 11: (a) The evolution of the average recrystallized grain area $\langle A \rangle$ through time for $\lambda = 18.5$ and 11.1 , respectively. The slope of two is predicted by the growth rate of a circle under pure bulk energy motion. Corresponds to Figure 8 of [33]. (b) The grain size distribution function for recrystallized grains for $\lambda = 3.7$ and 2000 site-saturated nuclei at $F = 0.9$. (c) The distribution of number of edges per grain for the same conditions as (b). (d) The mean normalized size of N_e sided grains for the same conditions as (b). (b), (c) and (d) correspond to Figures 10, 11, and 12 of [34], respectively.

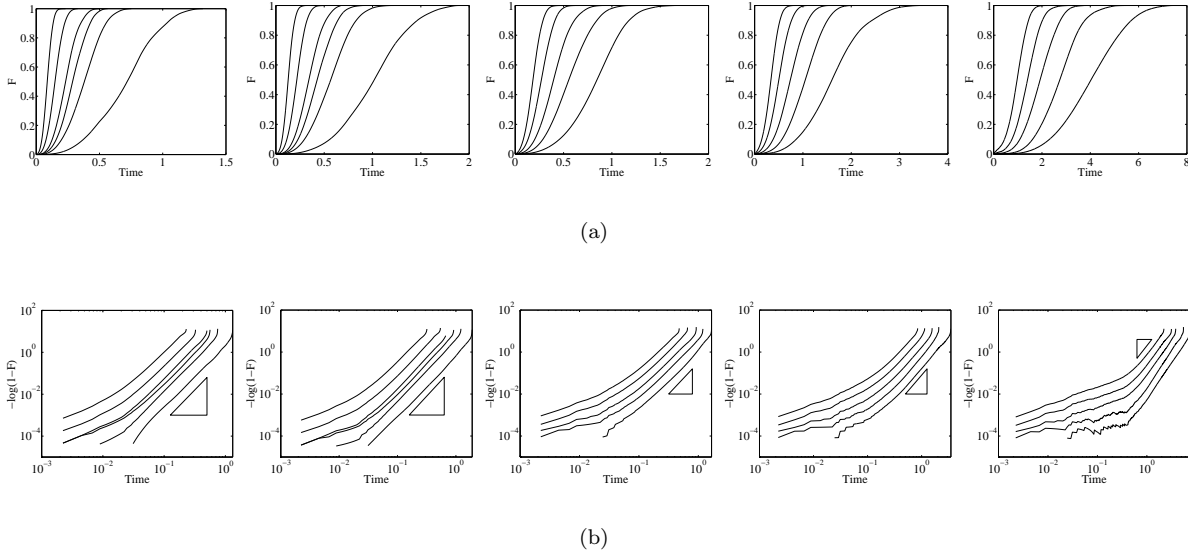


Figure 12: (a) The recrystallized area fraction F for $\lambda = 18.5, 11.1, 7.4, 5.55, 3.7$ and 1.85 , respectively. The curves correspond to 5607, 1121, 224, 112, 56, and 22 nucleations per unit time (from left to right) in the first two plots, and to 3364, 1121, 336, 112, and 37 nucleations per unit time in the last three. Corresponds to Figure 11 of [33] and Figure 18 of [34]. (b) The Avrami plots for the same experiments, corresponding to Figure 12 of [33] and Figure 19 of [34]. The slope of three is predicted for two-dimensional continuous nucleation.

Carlo steps of [33,34], as it is well known that some type of calibration must be performed to link Monte Carlo time to physical time (see, for instance, the discussion in [20], page 102). Based on the simulation times reported in this work and in [33,34] for site-saturated nucleation, we make the approximation that 1 nucleation per Monte Carlo step is roughly equivalent to 112.1 nucleations per unit time in our simulations.

Figure 12 displays the evolution of the recrystallized area fraction F in our simulations of continuous nucleation for choices of the parameter λ and the nucleation rate dn/dt , that correspond to those of Figures 11 and 12 of [33] and Figures 18 and 19 of [34]. In each case, it appears that the predicted Avrami exponent of 3 is approximately attained in the later stages of the simulation. Note that particularly for few nucleations per unit time and small λ , the Avrami plots are quite jagged early in the evolution. This is an effect of the small number of recrystallized nuclei present at this time in the simulation and the importance of the curvature term in delaying or preventing the growth of some nuclei (particularly for $\lambda = 3.7$ or 1.85 , which correspond to the heterogeneous nucleation regime).

In [33,34], the authors report that the recrystallized grain size for $F = 0.95$ varies with nucleation rate approximately as $(dn/dt)^{-2/3}$, in agreement with theoretical predictions of [14]. If we compare Figure 14 of [33] and Figure 15 of [34] to our Figure 13, then it is apparent that our simulations show good agreement with this prediction. Note that the last two data points for $\lambda = 18.5$ and 11.1 have areas averaged for less than 50 surviving recrystallized grains — such a small number of surviving grains is insufficient to expect close fit to statistical predictions.

5 Benefits of Diffusion-Generated Motion

As already mentioned, the work of Srolovitz et al. in [33,34] and of Hesselbarth and Göbel in [17] represent some of the major contributions to the field. There is a long list of more recent works that add further physical details (such as texture) to the models and extend the simulations to three dimensions (for example, [13,29]), but the basic Monte Carlo techniques remain largely the same. It is important to be aware of some basic

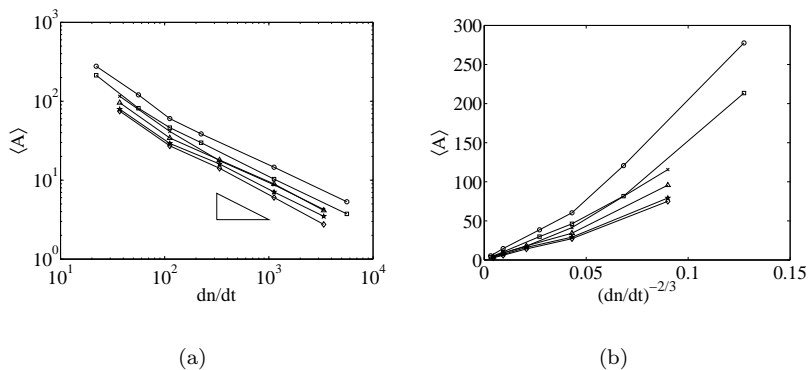


Figure 13: Comparison of the mean recrystallized grain size $\langle A \rangle$ at $F = 0.95$ to the nucleation rate dn/dt . $\lambda = 18.5, 11.1, 7.4, 5.55, 3.7$ and 1.85 correspond to circle, square, triangle, star, diamond and x markers, respectively.

limitations of the Monte Carlo technique applied in [33,34]:

- For small λ , [33,34] cannot produce the appropriate stationary shapes seen in Figure 4, with aspect ratio independent of λ .
- For large λ , grain boundaries become rough, though the PDE description of the model does not predict this behavior.
- Monte Carlo techniques are most appropriate for simulating atomistic-scale interactions. Recrystallization is often studied on the micrometer scale and so would require prohibitively expensive computation for each grid point to resolve the atomistic scale.
- The lattice definition (e.g. square or triangular) and neighborhood definition affect the results of Monte Carlo simulations, as noted in [1].

In Figures 1 and 2 of [34], the authors demonstrate that nuclei grow along grain boundaries but not out into the bulk of unrecrystallized grains for small values of the parameter H/J in their Monte Carlo simulations. However, we have shown in Section 3.2 that the critical grain shapes have aspect ratios independent of λ for this model: the shapes described in [34] are artifacts of the algorithm, not the model. In particular, we believe that they are a consequence of performing zero temperature simulations. For sufficiently small H/J in Monte Carlo simulations, it is *never* energetically favorable to change a single site from unrecrystallized to recrystallized if less than half the neighboring sites are already recrystallized. For certain parameter choices, it will be energetically favorable for growth to occur only along the grain boundary but not out into the unrecrystallized grain bulk. This observation is independent of the grid resolution and the overall size of the recrystallized grain which is attempting to grow. In contrast, Figure 3 shows that, under the diffusion-generated motion algorithm, any initial nucleus which is sufficiently large for the choice of λ will grow and evolve towards the critical shape described by Equation (7).

In [33], the authors forthrightly admit that rough boundaries arise from the growth of a circular grain for large H/J . Figure 3 demonstrates that no such difficulty arises for diffusion generated motion with precisely corresponding parameter choices. Though the initial shape is very irregular, it quickly relaxes to a shape with smooth boundary and maintains smooth boundaries away from triple junctions as $\lambda/\kappa \rightarrow \infty$. These observations suggest that the Monte Carlo model has limitations for *both* large and small values of H/J . However, diffusion generated motion successfully obtains the correct behaviors in both situations.

The two-dimensional simulations of [33,34] are performed on 200×200 grids. In three dimensions, [29] work on a $30 \times 30 \times 30$ grid, and [13] work on a grid of $100 \times 100 \times 100$ with 822 initial grains. In Sections 5.1 and 5.2, we perform much larger simulations in both two and three dimensions while at the same time having full benefit of subgrid resolution. These simulations take as initial condition a number of unrecrystallized

grains generated by normal grain growth starting from Voronoi initial data. The parameters for our two-dimensional simulations are chosen to agree with physically relevant length scales and surface tensions and bulk energies. In three dimensions, computational constraints prevent us from obtaining the proper scaling between unrecrystallized grains and recrystallizing nuclei (while having several unrecrystallized grains fit into the computational domain). We nucleate grains with mean radius $\langle r_n \rangle = 0.0378$, so that nuclei are approximately 5×10^{-5} the volume of unrecrystallized grains initially. The vast majority of the nuclei disappear quickly. We are able to see the influence of the angle conditions and surface tension on the microstructure (which always play a role at junctions and at small scales even when vanishingly small, as discussed in previous sections), resulting in grains which are clearly faceted as seen in experiments. In contrast, other numerical algorithms fail to show this clear faceting. The pure bulk energy phase field simulations of Bernacki et al. fail to respect the angle conditions (for example, see Figure 8 of [5]) and recrystallizing grains tend to be circular until collision with other recrystallizing grains. Monte Carlo simulations necessarily generate grains with rough boundaries, as discussed in [33], which also produces less clearly faceted grains.

As the discretization of a continuum (PDE) model, we believe that diffusion generation motion is more appropriate for simulating evolutions at the micrometer scale than the inherently atomistic Monte Carlo method. As such, our simulations can more cleanly reproduce theoretical predictions of the PDE model (5) used in this work. For example, the diffusion generated motion simulations correctly find the appropriate nucleation regimes for parameters in μ – R_1 space, while the Monte Carlo simulations fail to do so (see Figure 8). Furthermore, the diffusion generated motion algorithm performs correctly on a simple uniform grid and requires no definition of the neighborhood surrounding a grid point.

5.1 Large Scale Two-Dimensional Simulations

We present three large-scale simulations of recrystallization in two dimensions. Each simulation is initialized with sixteen unrecrystallized grains on a domain that corresponds to $D = [0, 4\sqrt{\pi}]^2$ in our nondimensionalized setting. In each simulation, tens of thousands to millions of recrystallized grains are nucleated, with initial sizes thousands of times smaller than the existing grains. The first two simulations are performed under site-saturated nucleation conditions, designed to demonstrate the ability of our algorithm to efficiently simulate recrystallization with physically-relevant parameter choices and to allow for comparison to the analysis of Section 3.3. The third simulation is performed under the conditions of continuous nucleation. Here, only 26 of over *four million* nuclei survive to the end of recrystallization, as the mean nucleus size is much smaller than the critical nuclei sizes described by Equation (10). The variation seen in grain sizes at the completion of recrystallization is primarily due to the differing nucleation times of the surviving grains. In contrast, the variation in grain sizes seen in the simulation with site-saturated nucleation is due primarily to differences in time of impingement along pre-existing grain boundaries.

5.1.1 Site-Saturated Nucleation I

In the first simulation we make physically reasonable choices for the sizes of recrystallizing nuclei and unrecrystallized grains. We choose $\lambda = 577.73$, and nucleate 42,095 grains. The radii of nuclei are normally distributed with mean $\langle r_n \rangle = 3.55 \times 10^{-4}$ and standard deviation $\sigma_n = 7.09 \times 10^{-5}$. This choice of parameters is well within the heterogeneous nucleation regime, as $R_1 = 1.73 \times 10^{-3}$. Using the values $\gamma = 0.5 J/m^2$ and $\rho = 10 MPa$ discussed in Section 1, $\langle r_0 \rangle = 28.9 \mu m$, and the mean recrystallizing nucleus size is $\langle r_n \rangle = 0.01 \mu m$: recrystallizing nuclei are a factor of 10^4 smaller than unrecrystallized grains. This wide range of length scales is necessary for curvature effects to be significant for recrystallizing nuclei while maintaining physical sizes for unrecrystallized grains. With these parameter choices, by the time a recrystallized nucleus reaches a size comparable to that of a pre-existing grain, the effect of surface tension will be negligible away from junctions (where angle conditions will still be maintained): along facets, the bulk energy term will dominate the dynamics.

We evolve until the nuclei completely cover D at $t = 1.73 \times 10^{-3}$. At that time, there are 245 surviving recrystallized grains. The vast majority of nucleated grains disappear almost immediately in the evolution. Figure 14 displays the agreement of this simulation with JMAK predictions. The recrystallized area fraction F evolves sigmoidally in time and the Avrami plot of t against $-\log(1 - F(t))$ appears to be approximately linear on logarithmic axes. The slope of the line in the Avrami plot is approximately 2, agreeing with

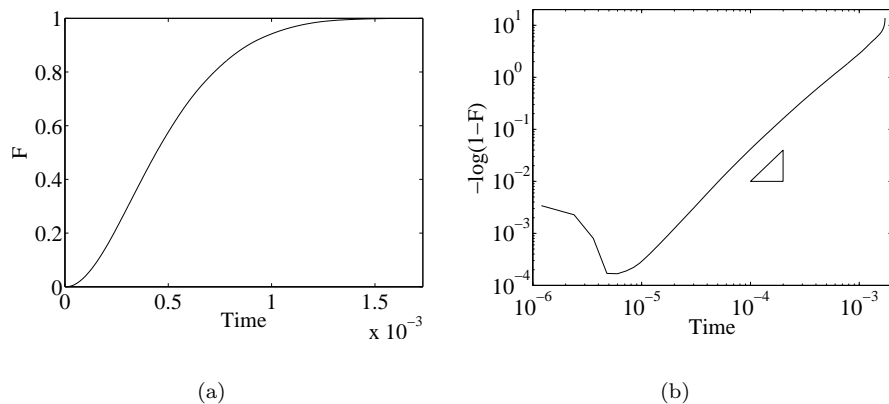


Figure 14: Recrystallization kinetics for two dimensional site-saturated nucleation with physically relevant parameters. (a) The fraction of recrystallized area F evolves sigmoidally in time, as expected. (b) The Avrami plot is approximately linear throughout the bulk of the evolution and demonstrates the expected slope of 2 for site-saturated homogeneous nucleation in two dimensions. The initial decrease in the Avrami plot is due to the fast disappearance of many nucleated grains that do not survive.

the prediction in [7] (page 542) for site-saturated homogeneous nucleation. There is a visible decrease in $-\log(1 - F)$ at early times. This is due to the large number of nuclei that are nucleated but disappear almost immediately.

For $\lambda = 577.73$, a circular recrystallizing grain contained within a single pre-existing grain must have its radius r be at least $0.05 \mu m$ in order to remain stationary. Smaller grains that are not touching each other or crossing grain boundaries will shrink and disappear. Recrystallizing nuclei crossing grain boundaries or touching other recrystallizing nuclei benefit both from the additional energy removed from the system (due to elimination of part of the original boundaries) and from the natural boundary conditions which take effect immediately, quickly forming the characteristic shape described in Section 3.1. This preference is displayed clearly in Figure 15(a), where at time $t = 1.07 \times 10^{-4}$, the surviving nuclei are primarily located along grain boundaries. Note that by this time the surviving recrystallized grains (which appear quite tiny) have already grown considerably from their initial embryonic state – the embryos are too small to display on this Figure 15(a). At this time, we also observe that large numbers of recrystallized grains that survive along existing grain boundaries contact their neighbors as they grow, and as a result of this crowding recrystallized grains tend to form elongated shapes which eventually penetrate deep into the bulk of unrecrystallized grains (see Figure 15(b), at time $t = 4.90 \times 10^{-4}$). When the evolution is complete, at $t = 1.73 \times 10^{-3}$, there are many elongated grains because the majority of surviving recrystallized grains nucleated at grain boundaries, and there are many more surviving recrystallized grains (245) than there were unrecrystallized grains originally (16). The Herring angle condition is maintained for the recrystallized grain pattern. This is difficult to see when the entire simulation domain D is viewed (Figure 15(c), top), as the surface tension term is negligible in comparison to the bulk energy term at the $O(1)$ scale with our choice of parameters. On smaller scales (same figure, zoomed in at bottom), the mere presence of the tiny surface tension introduces curvature into grain boundaries right near the junctions to maintain the Herring angle condition.

5.1.2 Site-Saturated Nucleation II

In this simulation, we choose parameters to predict even more severe heterogeneity than in the simulation of Section 5.1.1. We set $\lambda = 288.87$, and nucleate 162,070 grains. The radii of nuclei are normally distributed with mean $\langle r_n \rangle = 2.13 \times 10^{-3}$ and standard deviation $\sigma_n = 2.13 \times 10^{-4}$. Here, using the values $\gamma = 0.5 J/m^2$ and $\rho = 10 MPa$ determines that $\langle r_0 \rangle = 14.4 \mu m$, and the mean recrystallizing nucleus size is $\langle r_n \rangle = 0.03 \mu m$. These parameters are chosen to support successful nucleation along grain boundaries and at triple junctions while discouraging the survival of nuclei in pre-existing grain interiors. The number of grains expected to

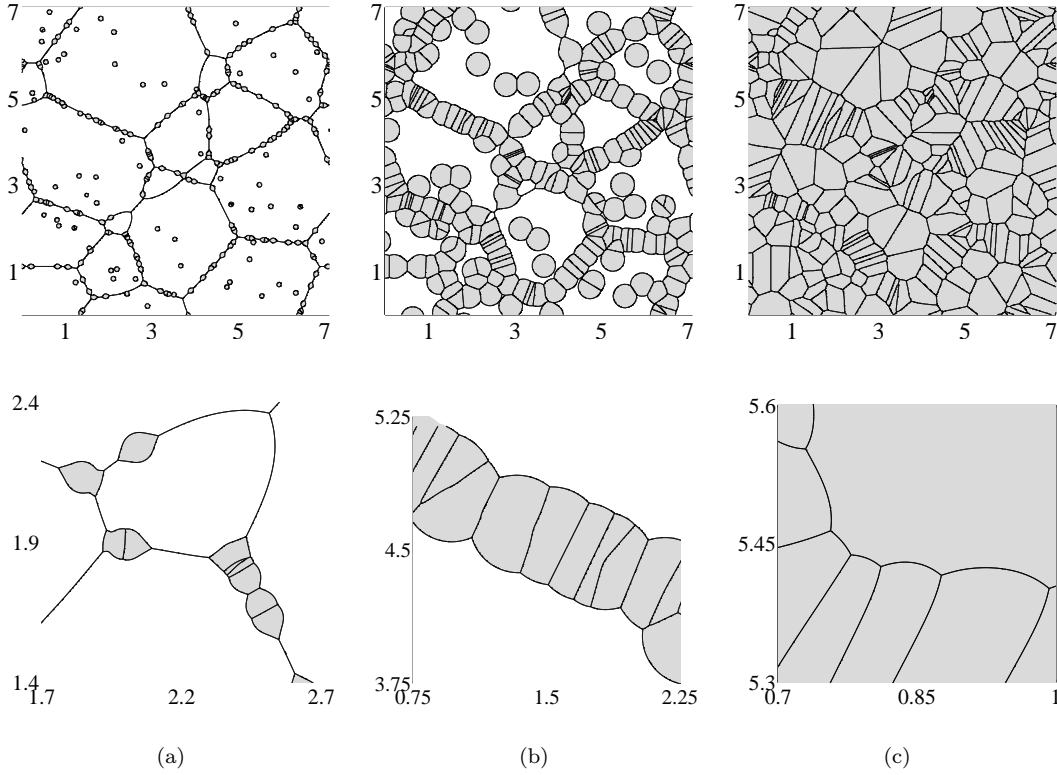


Figure 15: Microstructure of two-dimensional site-saturated nucleation simulation I, with physically relevant parameters. (a) At time $t = 1.07 \times 10^{-4}$, with $F = 0.05$. Surviving nuclei are heavily concentrated along grain boundaries. The originally-circular nuclei are clearly taking the characteristic shape described in Section 3.1. (b) At time $t = 4.90 \times 10^{-4}$, with $F = 0.56$. The concentration of surviving nuclei along the original grain boundaries leads to elongated recrystallizing grains as recrystallization continues. (c) Recrystallization is complete at time $t = 1.73 \times 10^{-3}$. Many elongated recrystallized grains are present because most surviving nuclei originated along grain boundaries. Close inspection reveals that recrystallized grain boundaries meet at 120° angles though this cannot be easily seen when viewing the entire simulation domain. At this level, the evolution is dominated by the bulk energy motion. Full simulation domain shown at top, with zoom-in below.

survive is higher than in the previous simulation. We evolve until the nuclei cover D at $t = 5.12 \times 10^{-3}$. At this time, there are 542 surviving recrystallized grains.

The simulation described in Section 5.1.1 approached the limit of the grid resolution. The mean nuclei radius was just 1.23 grid cells. This simulation further refines the grid, takes larger recrystallizing nuclei to improve resolution in the initial stages of the simulation, and decreases the value of λ . These changes allow for comparison with the theoretical predictions of Section 3.3, which depend on accurate computations for grains near the critical sizes. We discretize the initial condition on a 8192×8192 grid. After the surviving recrystallized grains grow to sufficient size, we coarsen the grid to 4096×4096 and take larger time steps. No impact on the kinetics of recrystallization were detected.

The analysis of Section 3.3 is rough, yet Equations (16) and (20) make excellent predictions for this simulation. Indeed, these equations indicate that nuclei should only survive along grain boundaries or at triple junctions, with 99.5% of surviving nuclei originally nucleating along grain boundaries and the remainder at triple junctions. Visual inspection of Figure 16 indicates that a few nuclei survive in the grain interior, but that the vast majority of survivors are indeed along grain boundaries and triple junctions. The analysis predicts that 0.02% of the nuclei should survive, agreeing reasonably well with the simulated survival rate of 0.033% at the end of recrystallization.

Figure 16 shows the microstructure of the evolution at various times throughout the simulation. As noted, the majority of grains survive along grain boundaries and at triple junctions. In Figure 16(a), at time $t = 7.79 \times 10^{-5}$, $F = 9.9 \times 10^{-3}$. The zoom-in indicates that the growing grains tend towards the characteristic shape shown in Figure 3. Figures 16(b), (c) and (d) correspond to $t = 2.40 \times 10^{-4}$ and $F = 0.086$, $t = 5.51 \times 10^{-4}$ and $F = 0.26$, and $t = 5.13 \times 10^{-3}$ and $F = 1$, respectively. As in the prior simulation, it can be seen that the Herring angle condition is maintained, though these boundary conditions are difficult to visualize on the scale of the full simulation (Figure 16(d)).

As recrystallization proceeds, grains begin to impinge upon each other along grain boundaries and grow primarily normal to the boundaries between pre-existing grains. Thus the recrystallized grains tend to be quite elongated. Figure 17(a) shows the distribution of a generalized measure of eccentricity computed among grains surviving at the completion of recrystallization. The generalized eccentricity is computed as the ratio of radius computed from perimeter, $R_P = (\text{Perimeter})/2\pi$, to radius computed from area, $R_A = \sqrt{(\text{Area})/\pi}$. Many of the grains remaining at the end of recrystallization have high eccentricity, greater than that of a rectangle with side length ratio of 10 : 1. The most eccentric grains had eccentricity comparable to a rectangle with side length ratio of 20 : 1. The mean grain eccentricity is 1.58, with standard deviation 0.41. In contrast, grain eccentricities were calculated for fifty smaller simulations of normal grain growth, each starting with approximately 10,000 grains initialized as Voronoi data and concluding with approximately 1,000 grains. For these simulations of normal grain growth, the final mean grain eccentricity is 1.06, with standard deviation 0.03.

Figure 17 compares the evolution of the recrystallized area fraction (F) with JMAK predictions. The recrystallized area fraction F is expected to be a sigmoidal function of time. In this simulation, the sigmoidal tails are asymmetric (Figure 17(b)). This effect is due to the multiple growth regimes clearly seen in the Avrami plot (Figure 17(c)). The prediction for site-saturated homogeneous nucleation is a slope of 2 [7] (page 542). This slope is seen early in the evolution, before nucleated grains begin to impinge upon each other in significant numbers. Later in the evolution, nucleated grains show significant impingement along the pre-existing grain boundaries, but are still free to grow along the normal direction to the grain boundaries. In Figure 17(c), the left triangle has a slope of 2, while the right triangle is fit locally to the data with a slope of 1.355.

After recrystallization concludes, the simulation reduces to normal grain growth (since the bulk energy terms in (5) vanish). Because surface tension is negligible away from triple junctions compared to the now exhausted bulk energy driving forces once the grains reach this scale, the evolution of the system becomes extremely slow and therefore the time step has to be increased in the simulation. We continue to coarsen the grid as the grain growth proceeds, allowing for computational efficiency with larger time steps. In doing so, we ensure that the mean grain width along the minor axis of the elongated grains remains well-resolved throughout the coarsening process. The final grid size is 1024×1024 . Recrystallization concludes at time $t = 5.13 \times 10^{-3}$, with 542 surviving nuclei. Grain growth is performed until just 52 grains remain, at time $t = 3.50 \times 10^{-1}$. A computation over such a long time period would be computationally infeasible without the grid and time step coarsening made possible by the large size of the surviving grains in the system, as

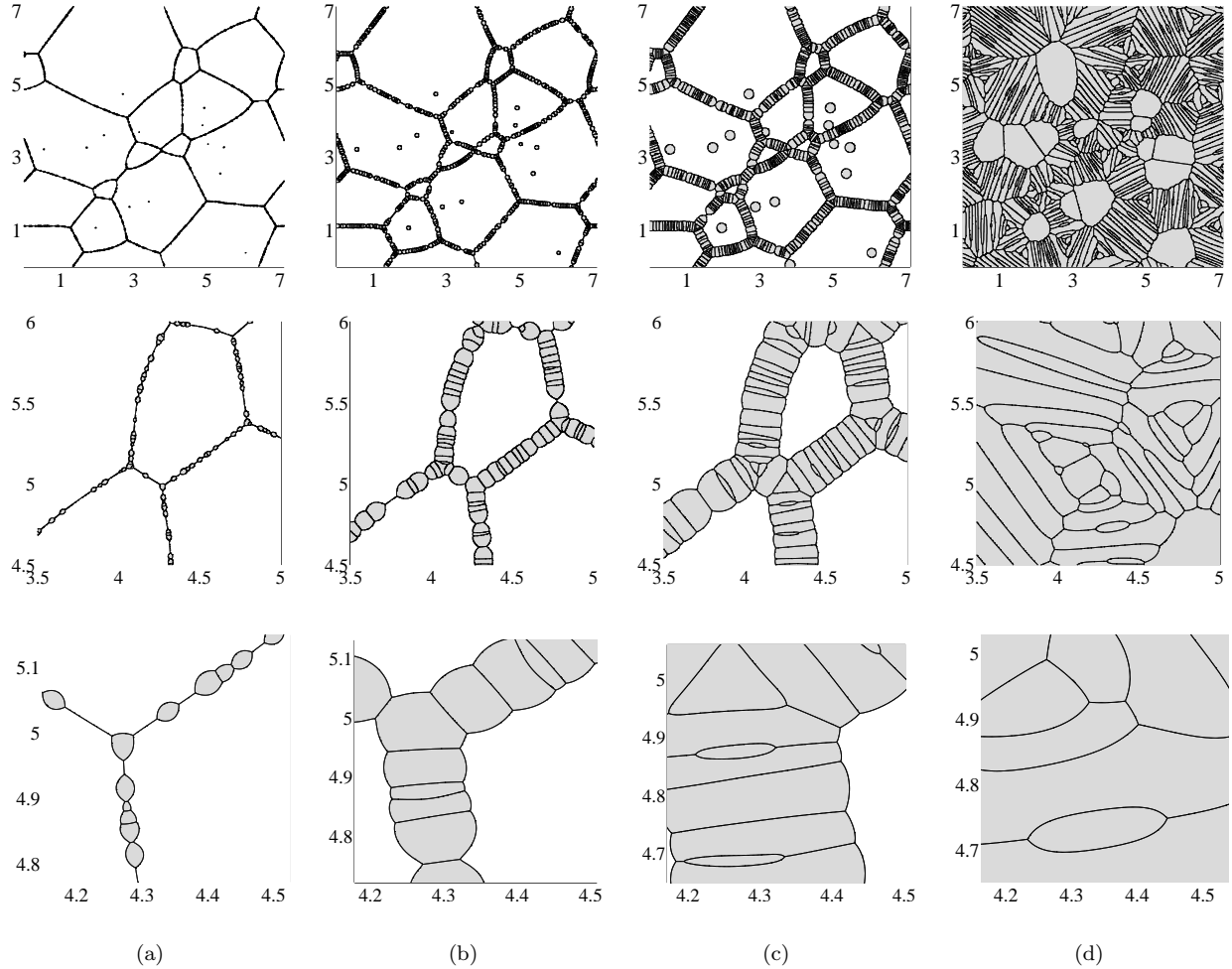


Figure 16: Microstructure of two-dimensional site-saturated nucleation simulation II, with higher surviving grain density along pre-existing grain boundaries. (a) At time $t = 7.79 \times 10^{-5}$, with $F = 9.9 \times 10^{-3}$. (b) At time $t = 2.40 \times 10^{-4}$, with $F = 0.086$. Nuclei are beginning to impinge along grain boundaries, while some unimpinged grains can still grow in all directions. (c) At time $t = 5.51 \times 10^{-4}$, $F = 0.26$. All nuclei except those in grain interiors have impinged along the pre-existing grain boundaries and can grow along only one dimension. (d) Recrystallization is complete at $t = 5.13 \times 10^{-3}$. Many elongated recrystallized grains are present because most surviving nuclei originated along grain boundaries. Full simulation domain shown at top, with successive magnification below.

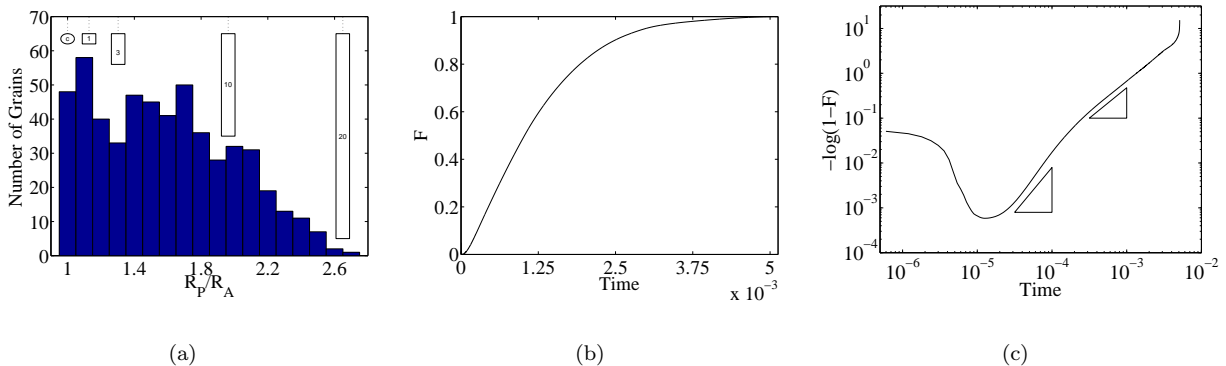


Figure 17: (a) The ratio of $R_P = (\text{Perimeter})/2\pi$ to $R_A = \sqrt{(\text{Area})/\pi}$ reveals that many grains are very elongated. For comparison, the value of R_P/R_A is shown for a circle and for rectangles with side length ratios of 1, 3, 10, and 20. (b) Recrystallization kinetics for two dimensional site-saturated nucleation with physically relevant parameters. The fraction of recrystallized area F evolves approximately sigmoidally in time. Two growth regimes are seen in the Avrami plot (c). The expected slope of 2 predicted for site-saturated homogeneous nucleation prevails initially. At later times, nuclei impinge along pre-existing grain boundaries but are free to grow in the direction normal to these boundaries. The data in this region is numerically fit to a slope of 1.355.

t	# Grains	$R(t)_{\max}$	$\langle R(t) \rangle$	$\psi(t)$	$\langle R_P/R_A \rangle$
5.13×10^{-3}	542	9.89×10^{-2}	2.10×10^{-2}	4.70	1.582
8.76×10^{-2}	161	1.40×10^{-1}	3.78×10^{-2}	3.72	1.196
1.76×10^{-1}	92	1.62×10^{-1}	4.97×10^{-2}	3.25	1.148
2.62×10^{-1}	66	1.75×10^{-1}	5.95×10^{-2}	2.93	1.138
3.50×10^{-1}	52	1.87×10^{-1}	6.68×10^{-2}	2.80	1.132

Table 2: Data for maximum grain size, mean grain size, and their ratio, $\psi(t)$ demonstrates that while $R(t)_{\max}$ increases, $\psi(t)$ decreases. $\psi(t) > 0$ is a condition for abnormal grain growth as defined by Detert [8]. The mean grain eccentricity $\langle R_P/R_A \rangle$ is also seen to decrease.

well as the unconditional numerical stability of our algorithms.

Figure 18 shows the evolution of the same microstructure from the simulation of Figure 16 beyond the fully recrystallized configuration shown in part (d) of that figure. More precisely, Figure 19(a), (b), and (c) show the solution, which evolves effectively via normal grain growth starting from Figure 16(d), at approximately quarter, half, and final times of the full computation. During this time, the elongated grains disappear or become more equiaxed. The few very large grains evident in the microstructure at the end of primary recrystallization continue to grow. Detert [8] defines *abnormal grain growth* as being characterized by an increase in maximum grain size that is much faster than the increase in mean grain size. Specifically, the function

$$\psi(t) = \frac{R(t)_{\max}}{\langle R(t) \rangle} \quad (23)$$

must be increasing. In this evolution, $R(t)_{\max}$ is increasing, but $\psi(t)$ is decreasing. Values at various stages in the evolution are shown in Table 2. This simulation result agrees with the conclusion of simulations in [32], and analysis in [36], in which the authors suggest that abnormal grain growth *cannot* occur under pure curvature motion, regardless of the initial grain size distribution. Instead, abnormal grain growth must result from additional factors such as the presence of second-phase particles, texture, or other surface effects ([18], page 316).

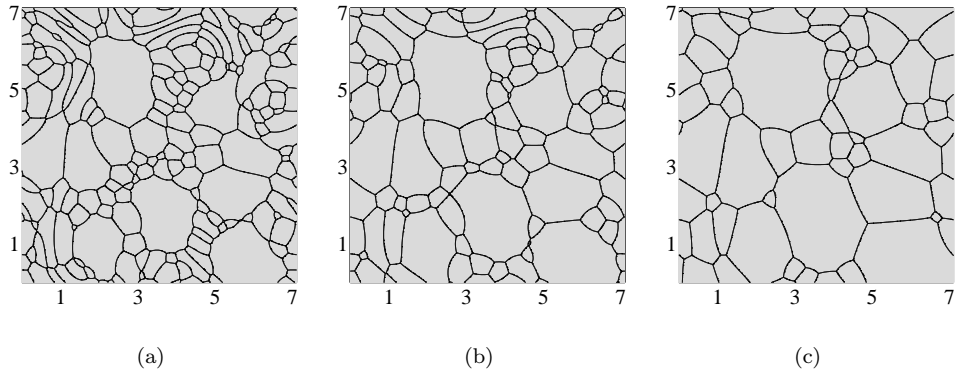


Figure 18: The evolution of the microstructure during grain growth following primary recrystallization at (a) $t = 8.76 \times 10^{-2}$, (b) $t = 1.76 \times 10^{-1}$, and (c) $t = 3.50 \times 10^{-1}$. Elongated grains tend to become more equiaxed. The unusually large grains continue to grow, but the mean grain size grows faster. This evolution does not correspond to abnormal grain growth.

Table 2 also displays the evolution of the mean grain eccentricity, $\langle R_P/R_A \rangle$. This value is also seen to decrease as normal grain growth proceeds. At the conclusion of the grain growth simulation, there are too few grains present to make statistically significant claims about the convergence of the grain size distribution to the self-similar distribution expected for normal grain growth (and which has been numerically observed by many authors, including the present ones, in dedicated simulations). However, the decay of both the maximum relative grain size $\psi(t)$ and the mean grain eccentricity towards values seen for normal grain growth (calculated as 2.212 and 1.06, respectively, for 50 simulations of normal grain growth from Voronoi initial data of approximately 10,000 grains until approximately 1,000 grains remain, via diffusion generated motion) suggests that this evolution is not significantly different that what is observed in typical simulations of normal grain growth, despite the highly unusual initial condition of extremely directionally-correlated and elongated grains.

5.1.3 Continuous Nucleation

The parameters in our continuous nucleation simulation have been chosen so that the vast majority of nuclei disappear quickly. Specifically, our parameters were: $\mu = 4.15 \times 10^{-3}$ and $\sigma = 1.21 \times 10^{-3}$, with $\lambda = 72.22$, corresponding to $R_1 = 1.39 \times 10^{-2}$, chosen so that R_1 lies eight standard deviations above the mean, with R_2 four standard deviations above the mean, and R_3 approximately two standard deviations above the mean. The nucleation rate is set to 3.5×10^8 nucleations per unit time. Throughout the full simulation, approximately 4.4 million grains are nucleated, but most do not survive.

The values $\gamma = 0.5 J/m^2$ and $\rho = 10 MPa$ determine that the mean unrecrystallized grain size for this simulation is $\langle r_0 \rangle = 3.61 \mu m$ and the mean recrystallized nucleus size is $\langle r_n \rangle = 0.015 \mu m$. Thus the unrecrystallized grains are somewhat smaller than often seen in experiment, but within an order of magnitude of the proper size. From Equations (16) and (20), we predict that no nuclei should survive away from grain boundaries, and that 43.5% of surviving nuclei are predicted to fall along grain boundaries, with the remaining 56.5% at triple junctions. This prediction is borne out well by Figure 19, though it is difficult to tell whether some surviving nuclei were touching grain boundaries at the time of nucleation. Further, we calculate $\mathbb{P}(G) \approx 4.13 \times 10^{-6}$. With 4.4 million total nucleations, the basic analysis of Section 3.3 predicts that approximately 18 of the nuclei will survive. Although our analysis in Section 3.3 does not account for continuous nucleation in any way — in particular, the changing proportion of grain boundaries in the simulation domain D is unaccounted for — and yet agrees quite well with the simulation result, in which there are 26 grains present when nucleation completes.

The final microstructure seen in Figure 19 is quite different than that seen in Figure 15, where the simulations took place under site-saturated nucleation. There are far fewer survivors due to the differing

parameter choices. The surviving grains tend to be more equiaxed in this simulation because the density of surviving nuclei along grain boundaries is much lower. Final recrystallized grain sizes vary greatly in both simulations, but the mechanisms behind this variation differ. In the site-saturated case, the variation is due to the variation in times when impingement occurs between recrystallizing grains along the pre-existing grain boundary. In the continuous case, the variation is explained primarily by the different times at which the surviving nuclei were nucleated.

Figure 20 demonstrates the evolution of the recrystallized area fraction F through time. The Avrami plot in Figure 20(b) clearly shows a long transition period before the expected Avrami exponent, 3, emerges. In this case, the initial increase in this plot is because nuclei are being added to the system (increasing F at a constant rate) faster than the nuclei present disappear due to surface tension effects (decreasing F at a rate approximately proportional to the number of nuclei present), until a sufficient number of nuclei are present for these competing effects to find an equilibrium. F remains approximately constant from $t = 5 \times 10^{-5}$ to $t = 7.5 \times 10^{-4}$. Only after a few nuclei successfully begin to grow does the Avrami exponent achieve the predicted value.

5.2 Three-dimensional recrystallization

In three dimensions, our simulation begins with 216 unrecrystallized grains. The domain is $D = [0, 9.67]^3$, discretized on a $256 \times 256 \times 256$ grid, $\lambda = 12.407$, and the final time for the simulation is $t = 0.1713$. Spherical recrystallized grains are nucleated with normally distributed radii, with mean $\langle r_n \rangle = 0.0378$ and standard deviation $\sigma_n = 0.0094$. 243,872 nuclei are placed in the simulation domain D . In this case, taking the physically relevant parameter choices $\gamma = 0.5 \text{ J/m}^2$ and $\rho = 10 \text{ MPa}$, we find that the mean unrecrystallized grain radius is $0.62 \mu\text{m}$ and the mean recrystallized grain radius is $0.0234 \mu\text{m}$. The mean unrecrystallized grain radius is unphysically small. A significantly larger grid and the attendant memory requirements would be necessary to simulate three-dimensional recrystallization for this many (approximately 200) physically realistic unrecrystallized grains while maintaining the unrecrystallized nucleus size.

Just as in two dimensions, the three-dimensional simulations agree well with the JMAK predictions, as shown in Figure 21. In three dimensions, the predicted Avrami slope is 3 for site-saturated nucleation. Figure 22 shows the evolution of the microstructure as evolution progresses. At $t = 5.02 \times 10^{-2}$, recrystallization is 10% complete. The surviving recrystallized grains are still much smaller on average than the unrecrystallized grains. 50% recrystallization occurs at $t = 8.45 \times 10^{-2}$. By this time, there are fewer surviving recrystallizing grains (158) than unrecrystallized grains (216), so the recrystallizing grains are slightly larger on average at 50% recrystallization. At all stages of the evolution, the recrystallizing grains are visibly faceted, consistent with the Herring angle condition even though as before surface tension is negligible compared to bulk energy along the faces of the recrystallizing grains by the time they have grown to be comparable to the length scale of the initial grain network.

Figure 23 compares the evolution of mean grain volume and mean number of faces for recrystallized and unrecrystallized grains through time. Early in the evolution, the recrystallizing grains are very small and have few faces as compared to the unrecrystallized grains. The bulk energy term allows some of the recrystallization nuclei to grow despite their small size and low number of faces. The present authors demonstrate in [11] that, for normal grain growth, a grain with few faces is, on average, likely to be a shrinking grain, in agreement with the inexact three-dimensional extension of the von Neumann–Mullins prediction given in [26].

6 Conclusions

We apply the algorithm developed in [10, 12] based on diffusion generated motion of signed distance functions to simulations of recrystallization in two and three dimensions. The use of this algorithm allows for fully-resolved simulations of the PDE-based version of the recrystallization model introduced in the seminal works of Srolovitz et al. [33, 34]. Due to the computational efficiency and subgrid resolution of this algorithm, we obtained previously unseen levels of detail in our simulations. This detail allows for the identification of some numerical artifacts in the Monte Carlo simulations of [33, 34], and thus for separation of these artifacts from features inherent to the model.

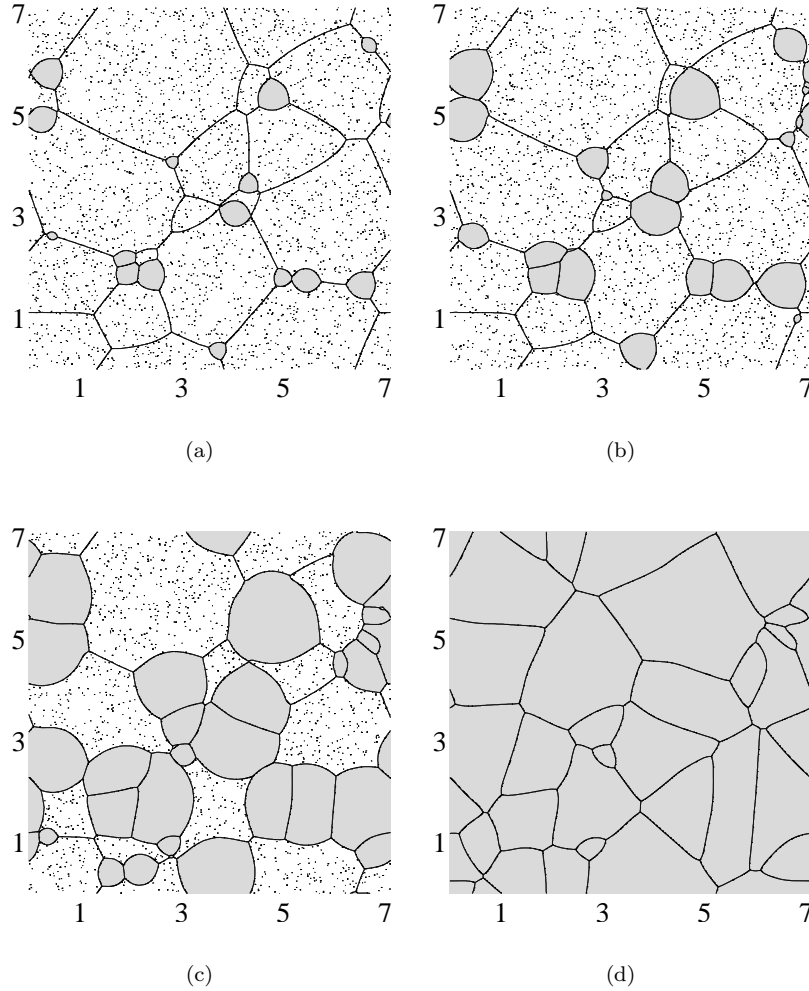


Figure 19: Microstructure from two-dimensional simulation with continuous nucleation. (a) At $t = 4.55 \times 10^{-3}$, with $F = 0.05$. All growing nuclei are located along grain boundaries or at triple junctions, as predicted. Many tiny nuclei can be seen throughout the microstructure. These nuclei have recently been nucleated but are not large enough to survive. (b) $F = 0.15$ at $t = 7.07 \times 10^{-3}$. Four new nuclei have successfully initiated visible growth since (a). All are quite small relative to the recrystallized grains that were also present in (a). (c) $F = 0.50$ at $t = 1.25 \times 10^{-2}$. Successful nuclei are of a wide variety of sizes, due to their varying nucleation times. Compare to Figure 15(b), where the nucleated grains are much closer in size, and size differences appear to be primarily due to impingement. (d) Recrystallization is complete at $t = 2.92 \times 10^{-2}$. The resultant grains are of a wide variety of sizes and shapes due to inhomogeneities in nucleation locations and varying nucleation times.

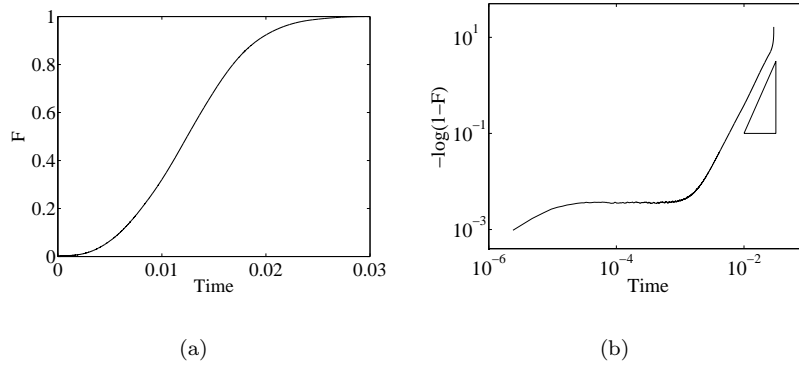


Figure 20: (a) The recrystallized area fraction F evolves sigmoidally as expected for the large-scale simulation of continuous nucleation in two dimensions. (b) The Avrami plot shows a long initial transition period in which nuclei are continuously placed in the microstructure but disappear at the same rate due to their small sizes and corresponding high curvatures. The expected Avrami exponent, 3, is seen at later times.

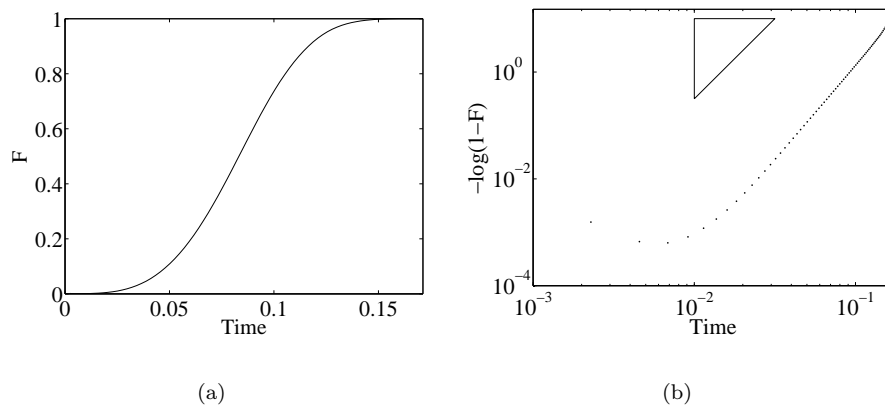
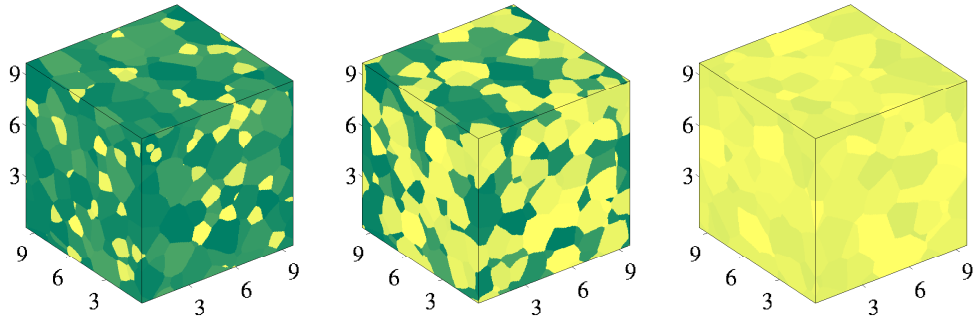
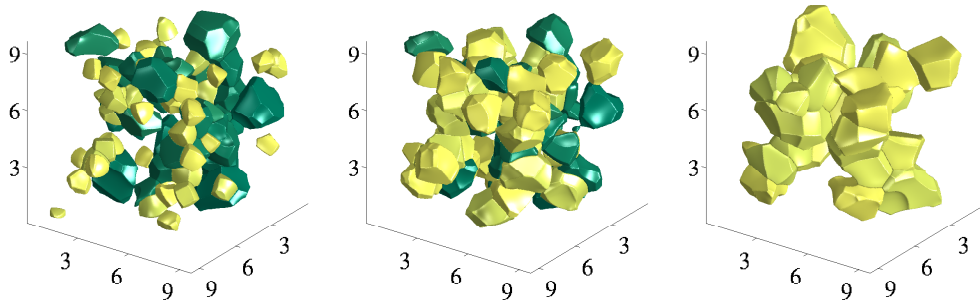


Figure 21: Recrystallized volume fraction F and Avrami plot for three-dimensional site saturated nucleation. (a) F evolves sigmoidally in time, as expected. (b) The Avrami plot is approximately linear throughout the bulk of the evolution and demonstrates the expected slope of 3 for site-saturated homogeneous nucleation in three dimensions.



(a)



(b)

Figure 22: (a) Surface planes at $F = 0.1$, $F = 0.5$, and $F = 1$, respectively. Recrystallizing grains are shown in shades of yellow, unrecrystallized grains in shades of green. (b) Subsets of grains are shown at the same points in the evolution. Note that recrystallizing grains are clearly faceted, and that at early times, recrystallizing grains appear to have fewer faces on average than the unrecrystallized grains.

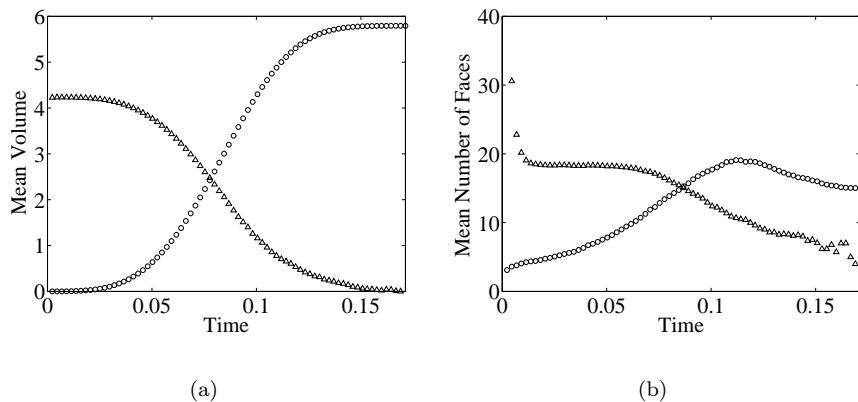


Figure 23: (a) Mean volume of recrystallized grains (circles) and of unrecrystallized grains (triangles) through time. (b) Mean number of faces among recrystallized (circles) and unrecrystallized (triangles) grains through time. Early in the evolution, recrystallized grains are quite small and are likely to meet less grains than the larger unrecrystallized grains. The bulk energy evolution causes the recrystallized grains to grow on average despite their smaller sizes and numbers of neighbors until the situation is reversed at later times.

Section 3 presents new analysis of the model. In particular, it is shown that surface tension effects are *always* important, even when the surface tension is vanishingly small in comparison to the bulk energy driving force. It is demonstrated that our algorithm capably captures the $O(1)$ effect described even for vanishingly small surface tensions and displays good agreement with the classification of parameter regimes presented here.

New simulations of recrystallization under this model are presented, with physically-relevant parameter choices. These parameter regimes could not be approached via the standard Monte Carlo method. For certain parameter choices in this range, we obtain microstructures at the conclusion of recrystallization composed primarily of extremely elongated grains. A simulation of three-dimensional grain growth is also presented. Though computational constraints prevent this simulation from taking physically-relevant parameters, good agreement with JMAK predictions is still obtained.

Acknowledgments

This work was supported, in part, by grants from the National Science Foundation: DMS-0748333 and DMS-0810113. Selim Esedođlu was also supported by an Alfred P. Sloan Foundation fellowship.

References

- [1] ANDERSON, M. P., SROLOVITZ, D. J., GRETT, G. S., AND SAHNI, P. S. Computer simulation of grain growth — I. Kinetics. *Acta Metall.* 32, 5 (1984), 783–791.
- [2] AVRAMI, M. Kinetics of phase change. I. General theory. *J. Chem. Phys.* 7 (1939), 1103–1112.
- [3] AVRAMI, M. Kinetics of phase change. II. Transformation-time relations for random distribution of nuclei. *J. Chem. Phys.* 8 (1940), 212–224.
- [4] AVRAMI, M. Kinetics of phase change. III. Granulation, phase change, and microstructure. *J. Chem. Phys.* 9, 2 (1941), 177–184.

- [5] BERNACKI, M., RESK, H., COUPEZ, T., AND LOGÉ, R. E. Finite element model of primary recrystallization in polycrystalline aggregates using a level set framework. *Model. Simul. Mater. Sci. Eng.* 17 (2009), 064006.
- [6] BURKE, J. E., AND TURNBULL, D. Recrystallization and grain growth. *Prog. Met. Phys.* 3 (1952), 220–292.
- [7] CHRISTIAN, J. W. *Theory of transformations in metals and alloys*, 2 ed. Pergamon, Oxford, 1975. (page 542).
- [8] DETERT, K. Secondary recrystallization. In *Recrystallization of Metallic Materials*, F. Haessner, Ed. Riederer Verlag, Stuttgart, 1978, p. 97.
- [9] DOHERTY, R. D., HUGHES, D. A., HUMPHREYS, F. J., JONAS, J. J., JENSEN, D. J., KASSNER, M. E., KING, W. E., MCNELLEY, T. R., MCQUEEN, H. J., AND ROLLETT, A. D. Current issues in recrystallization: a review. *Mater. Sci. Eng. A238* (1997), 219–274.
- [10] ELSEY, M., ESEDOĞLU, S., AND SMEREKA, P. Diffusion generated motion for grain growth in two and three dimensions. *J. Comp. Phys.* 228, 21 (2009), 8015–8033.
- [11] ELSEY, M., ESEDOĞLU, S., AND SMEREKA, P. Large scale simulation of normal grain growth via diffusion generated motion. To appear in *Proc. R. Soc. Lond. A* (2010).
- [12] ESEDOĞLU, S., RUUTH, S., AND TSAI, R. Diffusion generated motion using signed distance functions. *J. Comp. Phys.* 229, 4 (2010), 1017–1042.
- [13] FJELDBERG, E., AND MARTHINSEN, K. Computer simulations of kinetics and texture of recrystallisation by a 3-D Potts Monte Carlo model. *Mater. Sci. Forum* 558–559 (2007), 1069–1074.
- [14] GILBERT, E. N. Random subdivisions of space into crystals. *Ann. Math. Stat.* 33, 3 (1962), 958–972.
- [15] GOTTSTEIN, G., AND SHVINDLERMAN, L. *Grain Boundary Migration in Metals*. CRC Press, Boca Raton, Florida, 1999. (page 130).
- [16] HERRING, C. Surface tension as a motivation for sintering. In *The Physics of Powder Metallurgy*, W. Kingston, Ed. McGraw–Hill, New York, 1951, pp. 143–179.
- [17] HESSELBARTH, H. W., AND GÖBEL, I. R. Simulation of recrystallization by cellular automata. *Acta Metall. Mater.* 39, 9 (1991), 2135–2143.
- [18] HUMPHREYS, F. J., AND HATHERLY, M. *Recrystallization and Related Annealing Phenomena*, 1 ed. Pergamon, Oxford, 1995. (pages 8, 316, 422).
- [19] HURLEY, P. J., AND HUMPHREYS, F. J. Modelling the recrystallization of single-phase aluminum. *Acta Mater.* 51 (2003), 3779–3793.
- [20] JANSSENS, K. G. F., RAABE, D., KOZESCHNIK, E., MIODOWNIK, M. A., AND NESTLER, B. *Computational Materials Engineering*. Elsevier, London, 2007. (page 102).
- [21] JOHNSON, W. A., AND MEHL, R. F. Reaction kinetics in processes of nucleation and growth. *Trans. Am. Inst. Min. Metall. Eng.* 135 (1939), 416–442.
- [22] KOLMOGOROV, A. N. On the statistical theory of crystallization in metals. *Bull. Acad. Sci. USSR. Ser. Math.* 3 (1937), 367–368.
- [23] MARX, V., REHER, F. R., AND GOTTSTEIN, G. Simulation of primary recrystallization using a modified three-dimensional cellular automaton. *Acta Mater.* 47, 4 (1999), 1219–1230.
- [24] MERRIMAN, B., BENICE, J. K., AND OSHER, S. Motion of multiple junctions: a level set approach. *J. Comput. Phys.* 112, 2 (1994), 334–363.

- [25] MULLINS, W. W. Two-dimensional motion of idealized grain boundaries. *J. Appl. Phys.* 27, 6 (1956), 900–904.
- [26] MULLINS, W. W. Estimation of the geometrical rate constant in idealized three dimensional grain growth. *Acta Metall.* 37, 11 (1989), 2979–2984.
- [27] RAABE, D. Cellular automata in materials science with particular reference to recrystallization simulation. *Annu. Rev. Mater. Res.* 32 (2002), 53–76.
- [28] RADHAKRISHNAN, B., SARMA, G. B., WEILAND, H., AND BAGGETHUN, P. Simulations of deformation and recrystallization of single crystals of aluminum containing hard particles. *Modelling Simul. Mater. Sci. Eng.* 8, 5 (2000), 737–750.
- [29] RADHAKRISHNAN, B., SARMA, G. B., AND ZACHARIA, T. Modeling the kinetics and microstructural evolution during static recrystallization — Monte Carlo simulation of recrystallization. *Acta Mater.* 46, 12 (1998), 4415–4433.
- [30] REITICH, F., AND SONER, H. M. Three-phase boundary motion under constant velocities. I: The vanishing surface tension limit. *Proc. R. Soc. Edin.* 126A (1996), 837–865.
- [31] ROLLETT, A. D., AND RAABE, D. A hybrid model for mesoscopic simulation of recrystallization. *Comput. Mater. Sci.* 21 (2001), 69–78.
- [32] SROLOVITZ, D. J., GRETT, G. S., AND ANDERSON, M. P. Computer simulation of grain growth — V. Abnormal grain growth. *Acta Metall.* 33, 12 (1985), 2233–2247.
- [33] SROLOVITZ, D. J., GRETT, G. S., AND ANDERSON, M. P. Computer simulation of recrystallization — I. Homogeneous nucleation and growth. *Acta Metall.* 34, 9 (1986), 1833–1845.
- [34] SROLOVITZ, D. J., GRETT, G. S., ANDERSON, M. P., AND ROLLETT, A. D. Computer simulation of recrystallization — II. Heterogeneous nucleation and growth. *Acta Metall.* 36, 8 (1988), 2115–2128.
- [35] TAYLOR, J. E. The motion of multiple-phase junctions under prescribed phase-boundary velocities. *J. Differ. Equ.* 119 (1995), 109–136.
- [36] THOMPSON, C. V., FROST, H. J., AND SPAEPEN, F. The relative rates of secondary and normal grain growth. *Acta Metall.* 35, 4 (1987), 887–890.